

Intrinsic dopamine and acetylcholine dynamics in the striatum of mice

<https://doi.org/10.1038/s41586-023-05995-9>

Received: 8 June 2022

Accepted: 22 March 2023

Published online: 09 August 2023

 Check for updates

Anne C. Krok^{1,2}, Marta Maltese^{1,2,5}, Pratik Mistry^{1,2,5}, Xiaolei Miao^{3,4}, Yulong Li⁴ & Nicolas X. Tritsch^{1,2}✉

External rewards such as food and money are potent modifiers of behaviour^{1,2}. Pioneering studies established that these salient sensory stimuli briefly interrupt the tonic discharge of neurons that produce the neuromodulators dopamine (DA) and acetylcholine (ACh): midbrain DA neurons (DANs) fire a burst of action potentials that broadly elevates DA in the striatum^{3,4} at the same time that striatal cholinergic interneurons (CINs) produce a characteristic pause in firing^{5,6}. These phasic responses are thought to create unique, temporally limited conditions that motivate action and promote learning^{7–11}. However, the dynamics of DA and ACh outside explicitly rewarded situations remain poorly understood. Here we show that extracellular DA and ACh levels fluctuate spontaneously and periodically at a frequency of approximately 2 Hz in the dorsal striatum of mice and maintain the same temporal relationship relative to one another as that evoked by reward. We show that this neuromodulatory coordination does not arise from direct interactions between DA and ACh within the striatum. Instead, we provide evidence that periodic fluctuations in striatal DA are inherited from midbrain DANs, while striatal ACh transients are driven by glutamatergic inputs, which act to locally synchronize the spiking of CINs. Together, our findings show that striatal neuromodulatory dynamics are autonomously organized by distributed extra-striatal afferents. The dominance of intrinsic rhythms in DA and ACh offers new insights for explaining how reward-associated neural dynamics emerge and how the brain motivates action and promotes learning from within.

Rewards and the sensory cues that predict their availability elicit brief changes in release of the neuromodulators dopamine (DA) and acetylcholine (ACh). These phasic responses are thought to stand out from the basal, steady concentration of DA and ACh in which brain circuits are normally bathed to affect behaviour. In the mammalian striatum, rewards evoke a phasic increase in extracellular DA^{3,4} and a phasic decrease in ACh^{5,6}, the coincidence of which is critical for DA to act as a teaching signal, as muscarinic M4 receptors oppose D1 receptor-dependent synaptic plasticity on direct-pathway striatal projection neurons (SPNs)^{12,13}. Recent studies have also implicated phasic DA elevations in the initiation and invigoration of self-paced movements^{14–17}, and ACh has been proposed to help striatal circuits distinguish between DA signals related to motor performance and learning^{9–11,18,19}. However, the dynamics of extracellular DA and ACh levels in vivo remain unknown. Because DA and ACh interact extensively in the striatum without necessarily engaging somatic spiking^{20–25}, addressing this question requires approaches that directly and simultaneously report DA and ACh levels on sub-second time scales.

To reveal the dynamics of striatal DA and ACh, we imaged the D2 receptor-based red fluorescent GRAB-DA indicator rDA1m²⁶ and the

muscarinic M3 receptor-based green fluorescent GRAB-ACh indicator ACh3.0 (ref. 27) concurrently from the dorsolateral striatum (DLS) of mice head-fixed on a cylindrical treadmill using fibre photometry (Fig. 1a and Extended Data Fig. 1). These sensors display comparable kinetics in the hundred-millisecond range when reporting striatal release of DA and ACh in vivo²⁶ (Extended Data Fig. 2). Mice spontaneously alternated between bouts of immobility and locomotion and, on a subset of recording sessions, were provided with uncued water rewards. As expected, rewards evoked phasic changes in the fluorescence of both sensors, reminiscent of the characteristic discharge of midbrain DA neurons (DANs)^{3,4} and striatal cholinergic interneurons (CINs)^{5,6} (Fig. 1b–e and Extended Data Fig. 3). On average, rDA1m showed a sharp increase in fluorescence (mean (\pm s.e.m.) amplitude, $9.9\% \pm 1.0\% \Delta F/F$; $n = 13$ mice) that decayed back to baseline within 1.5 s, whereas ACh3.0 showed a phasic dip in fluorescence below a stable baseline (mean amplitude, $-4.4\% \pm 0.5\% \Delta F/F$; mean duration, 298 ± 21 ms) preceded by a brief increase in fluorescence (mean amplitude, $2.9\% \pm 0.7\% \Delta F/F$). These events appeared in a sequence, starting with the ACh3.0 peak followed 82 ± 5 ms later by the rDA1m peak, which itself was followed by the dip in ACh3.0 fluorescence (time to trough, 200 ± 17 ms) (Fig. 1f,g).

¹Neuroscience Institute, New York University Grossman School of Medicine, New York, NY, USA. ²Fresco Institute for Parkinson's and Movement Disorders, New York University Langone Health, New York, NY, USA. ³Department of Anesthesiology, Beijing Chao-Yang Hospital, Capital Medical University, Beijing, China. ⁴State Key Laboratory of Membrane Biology, Peking University School of Life Sciences, Beijing, China. ⁵These authors contributed equally: Marta Maltese, Pratik Mistry. ✉e-mail: nicolas.tritsch@nyulangone.org

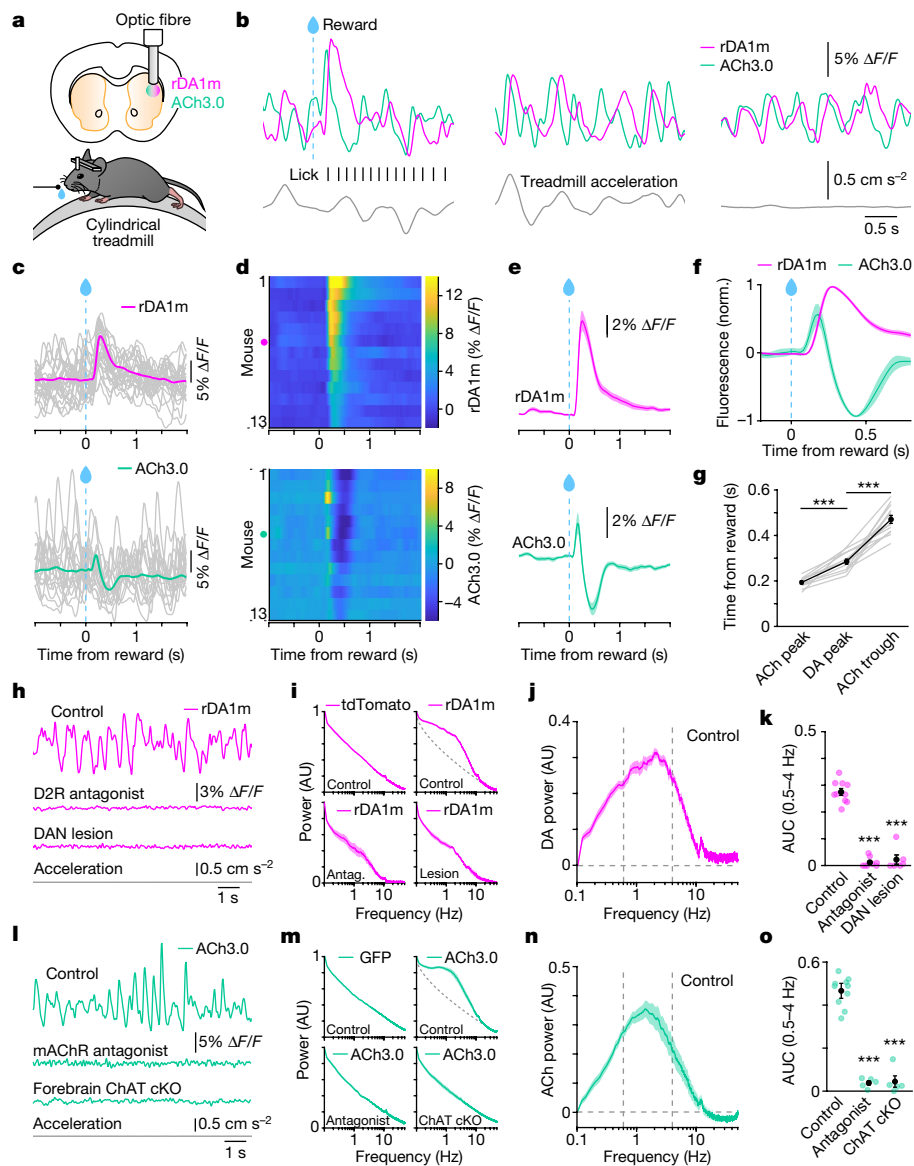


Fig. 1 | Spontaneous periodic fluctuations in striatal DA and ACh.
a, Experimental set-up to monitor DA and ACh levels in the DLS. **b**, Example rDA1m (magenta) and ACh3.0 (teal) fluorescence recorded during reward (left), locomotion (middle) and immobility (right). Black, licks; grey, treadmill acceleration. **c–e**, Session-averaged rDA1m (top) and ACh3.0 (bottom) signals aligned to solenoid valve opening (blue) in an example mouse (**c**; 20 randomly selected single trials shown in grey), in all recorded mice (**d**; animal in **c** indicated by a dot) and averaged across all 13 mice (**e**). **f**, Same as **e** normalized to rDA1m maxima and ACh3.0 minima. **g**, Latency of reward-evoked DA and ACh transients (ACh peak versus DA peak, $P = 2.5 \times 10^{-7}$; DA peak versus ACh trough, $P = 9.6 \times 10^{-10}$; one-way balanced ANOVA, Dunn's multiple-comparisons test; $n = 13$ mice). Data for individual mice are shown in grey. **h**, Example rDA1m fluorescence during immobility (top), following systemic treatment with the

D2R antagonist sulpiride (middle) or following midbrain DAN lesion with 6-OHDA (bottom). Acceleration for the control recording is shown in grey. **i**, Normalized power spectra of the photometry signal for tdTomato ($n = 3$ mice) and rDA1m in control ($n = 13$), sulpiride-treated ($n = 8$) and 6-OHDA-lesioned ($n = 6$) mice during immobility. AU, arbitrary units. **j**, Isolated power spectrum of DA signal. Vertical lines indicate 0.5 and 4 Hz. **k**, Area under the curve (AUC) for DA power in the band at 0.5–4 Hz in control ($n = 13$), sulpiride-treated ($P = 1.2 \times 10^{-12}$; $n = 8$) and 6-OHDA-lesioned ($P = 1.1 \times 10^{-9}$; $n = 6$) mice (all compared with control, Student's two-sample *t* test). **l–o**, Same as **h–k** for ACh3.0 in control ($n = 13$), scopolamine-treated ($P = 3.0 \times 10^{-6}$; $n = 5$) and ChAT cKO^{forebrain} ($P = 8.3 \times 10^{-6}$; $n = 5$) mice. Group means (\pm s.e.m.) in **g**, **k**, **o** are shown in black. Shaded areas in **e**, **f**, **i**, **j**, **m**, **n** depict s.e.m. * $P < 0.05$, ** $P < 0.01$ and *** $P < 0.001$.

These data are consistent with the sequence of reward-evoked action potential responses observed from putative DANs and CINs in rodents and primates^{3–6}.

The fluorescence of rDA1m and ACh3.0 also increased during locomotion, with ACh3.0 peaking near the time of maximum positive acceleration and rDA1m peaking shortly thereafter (Fig. 1b and Extended Data Fig. 4), in line with recent reports using genetically encoded calcium indicators to monitor the activity of midbrain DANs and striatal CINs in mice^{14,19}. Together, these data confirm our ability to detect and isolate

phasic changes in striatal DA and ACh from simultaneous photometric recordings.

DA and ACh fluctuate spontaneously

rDA1m and ACh3.0 fluorescence signals also showed large, periodic fluctuations during periods of immobility and in the absence of overt sensory stimuli that were not apparent in session-averaged data (Fig. 1b,c,h,l and Extended Data Fig. 3a,m,n). These spontaneous

signal fluctuations, which occurred most prominently in the frequency band at 0.5–4 Hz (mode for DA, 2.0 ± 0.2 Hz; mode for ACh, 1.8 ± 0.2 Hz; Fig. 1j,n) were also observed before mice ever received rewards on the treadmill as well as in an open-field arena (Extended Data Fig. 5), but not in mice expressing green fluorescent protein (GFP) or tdTomato (Fig. 1i,m), confirming that they do not reflect haemodynamic, movement or signal processing artefacts. In mice expressing rDA1m alone, spontaneous fluorescence transients during immobility were reversibly blocked following systemic administration of the D2 receptor (D2R) antagonist sulpiride ($n = 8$ mice) and were entirely absent following infusion of the toxin 6-hydroxydopamine (6-OHDA) in the substantia nigra pars compacta (SNc; $n = 6$ mice; Fig. 1h,i,k), showing that rDA1m fluorescence transients during immobility reflect DA release from midbrain DANs. In ACh3.0-expressing mice, spontaneous fluorescence transients disappeared following treatment with the muscarinic ACh receptor (mAChR) antagonist scopolamine ($n = 5$ mice) and were not detected in mice in which the ACh synthetic enzyme choline acetyltransferase (ChAT) was conditionally knocked out in forebrain cholinergic neurons (*ChAT^{lox/flox};Nkx2.1^{Cre}* mice, referred to hereafter as ChAT cKO_{forebrain} mice; $n = 5$ mice; Fig. 1l,m,o), indicating that ACh3.0 fluctuations reflect spontaneous changes in ACh release from local CINs and not brainstem cholinergic afferents. Together, these data show that striatal circuits constantly undergo large, periodic increases and decreases in extracellular DA and ACh levels originating from midbrain DAN axons and striatal CINs, respectively.

DA and ACh are constantly phase shifted

Striatal neurons coexpress receptors for DA and ACh that engage competing intracellular signalling pathways^{12,13,28}. The net impact of phasic changes in DA and ACh levels on striatal function therefore depends on their relative timing and amplitude. During rewards, DA and ACh were negatively correlated (Pearson's cross-correlation coefficient $r = -0.48 \pm 0.02$; $n = 13$ mice) with a temporal lag of 123 ± 9 ms (Fig. 2a–c), indicating that peaks in DA slightly precede dips in ACh. Notably, DA and ACh showed a similar negative correlation outside of reward, whether mice were actively locomoting or remained immobile (Fig. 2a–c and Extended Data Figs. 4h and 5b–d). In agreement with this, we observed strong coherence between DA and ACh in the frequency band at 0.5–4 Hz (Fig. 2d,e and Extended Data Fig. 5e,f) that maintained a phase offset of approximately 90 degrees (Fig. 2f–j and Extended Data Fig. 5g–k). By contrast, the mean amplitude of DA and ACh fluctuations differed between immobility, locomotion and reward, with the largest DA and ACh transients occurring during reward and locomotion, respectively (Fig. 2h,i), despite considerable variability and overlap in the amplitude distribution of individual transients (Extended Data Fig. 3a,m,n). These data therefore show that DA and ACh transients maintain a consistent temporal relationship across behavioural states and suggest that rewards and movements do not create a unique sequence of neuromodulatory events in the striatum, but instead recruit intrinsically structured rhythms in DA and ACh that are also manifest during periods of rest.

DA–ACh coherence is strongest locally

To determine whether stereotyped coupling between DA and ACh extends to other striatal regions, we coexpressed and simultaneously imaged rDA1m and ACh3.0 in the DLS as well as in the dorsomedial striatum (DMS; Extended Data Fig. 6a). Within the DMS, extracellular DA and ACh levels were negatively correlated, fluctuated constantly and coherently at 0.5–4 Hz, and were consistently phase shifted relative to one another, irrespective of behavioural state (Extended Data Fig. 6b–j), showing that DA and ACh maintain a similar temporal relationship in the DMS as in the DLS. To determine whether these fluctuations occur concurrently throughout the dorsal striatum, we compared DA

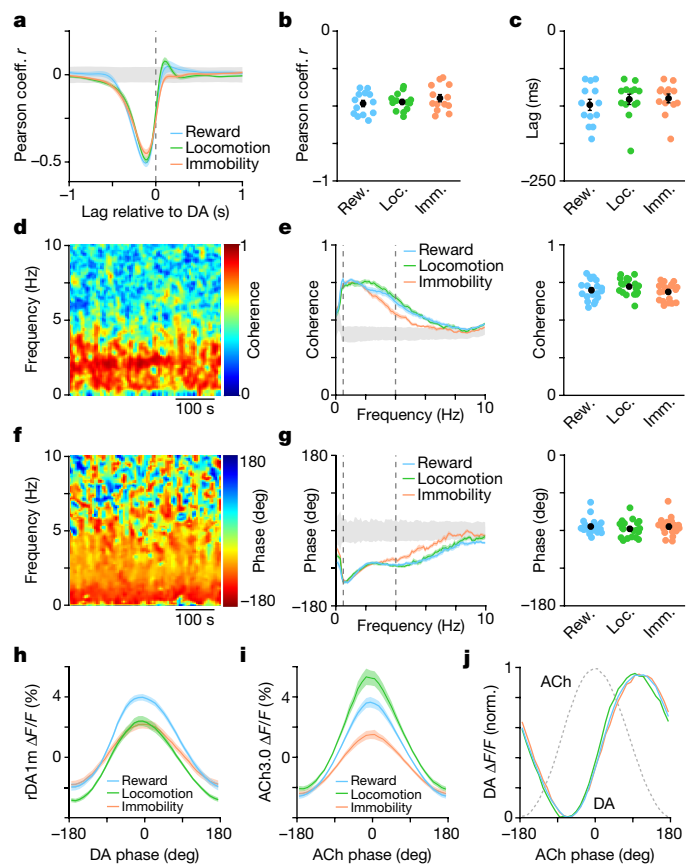


Fig. 2 | DA and ACh maintain a consistent temporal relationship across behavioural states. **a**, Mean cross-correlation between simultaneously recorded DA and ACh signals ($n = 13$ mice) during reward (blue), locomotion (green) and immobility (orange). The 95% confidence interval (CI) is shown in grey. **b**, Peak Pearson's correlation coefficient r between DA and ACh across behavioural states ($P = 0.5$, one-way balanced ANOVA; $n = 13$ mice). **c**, Same as **b** for the time lag of the negative cross-correlation peak ($P = 0.6$). **d**, Example coherence between DA and ACh signals across frequency and time domains. **e**, Left, mean coherence between DA and ACh at different frequencies across behavioural states ($n = 13$ mice). Vertical lines depict 0.5 and 4 Hz. Right, median coherence in the band at 0.5–4 Hz in individual mice ($P = 0.9$, one-way balanced ANOVA). **f,g**, Same as **d,e** for phase offset between DA and ACh ($P = 0.6$). **h**, Mean DA fluorescence at different phases of periodic DA fluctuations in the frequency band at 0.5–4 Hz. **i**, Same as **h** for ACh fluorescence. **j**, Peak normalized DA fluorescence versus phase of periodic ACh fluctuations (grey dashed line) in the band at 0.5–4 Hz during reward (blue), locomotion (green) and immobility (orange). Group means (\pm s.e.m.) in **b,c,e,g** are shown in black. Shaded areas in **a,e,g,h–j** depict s.e.m.

transients in one striatal region to ACh signals in the other. DA and ACh transients were not coherent between the DLS and DMS (Extended Data Fig. 6k,l), indicating that DA and ACh are not entrained by global, brain-wide rhythms such as breathing. Thus, although DA and ACh are stereotypically coupled locally, periodic fluctuations in the DLS are not synchronous with those in the DMS.

DA and ACh are not coordinated locally

Experiments in brain slices have convincingly demonstrated that DA release can briefly pause CIN firing through D2Rs^{24,25}, while synchronous activation of CINs can evoke action potentials in DAN axons and cause widespread release of DA in the striatum following the activation of presynaptic β 2-containing nicotinic ACh receptors (nAChRs)^{20–23}. Thus, local coordination between DA and ACh may result from direct intra-striatal interactions between these neuromodulators.

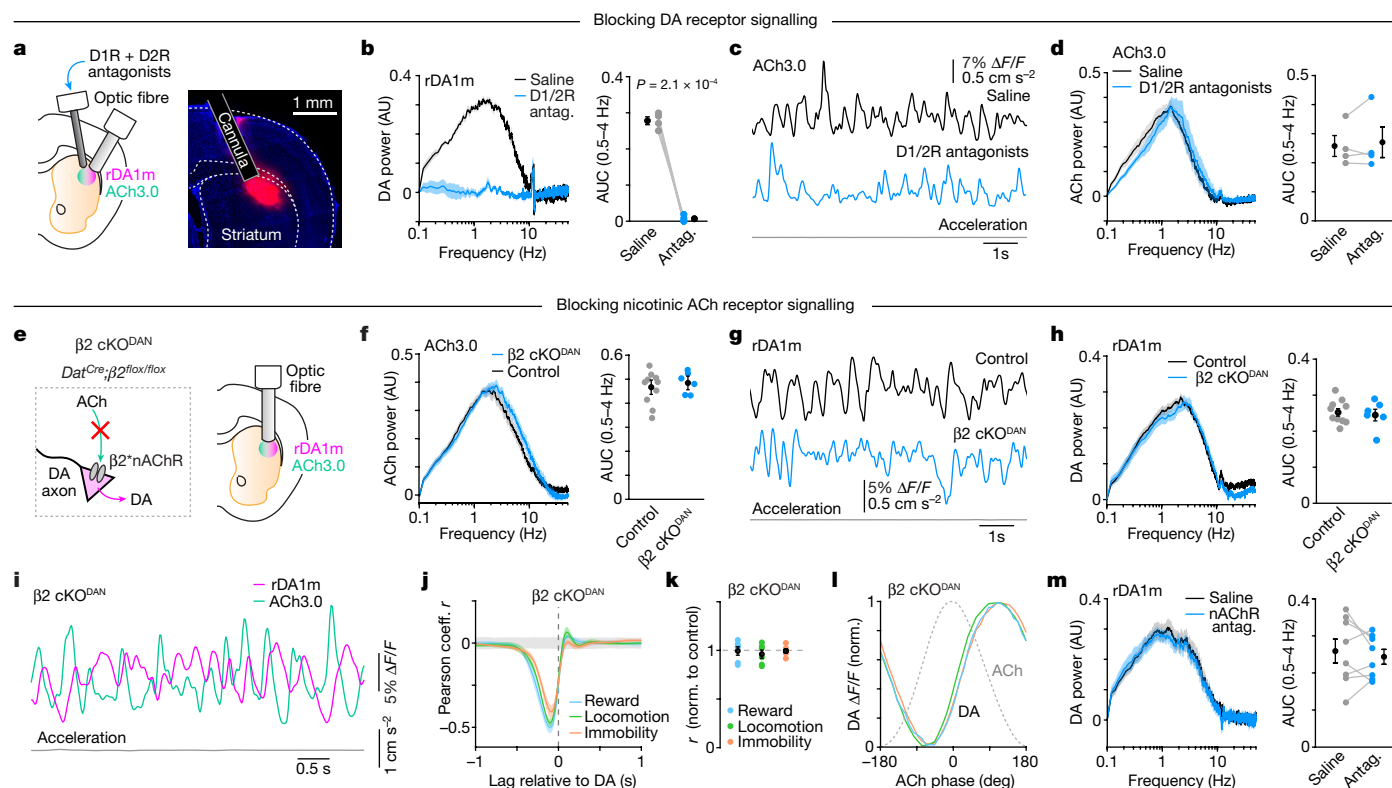


Fig. 3 | Periodic DA and ACh fluctuations are not coordinated locally in the striatum. **a**, Left, experimental preparation. Right, drug diffusion estimate using fluorescent dye in one of three similar experiments. **b**, Mean DA power spectrum (left) and AUC in the band at 0.5–4 Hz (right; $P = 2.1 \times 10^{-4}$, Student's paired t test; $n = 4$ mice) during immobility after intra-striatal infusion of saline (black) or D1 and D2 receptor (D1/2R) antagonists (blue). **c**, Example ACh3.0 recording in saline or D1/2R antagonists. **d**, Same as **b** for ACh ($P = 0.35$). **e**, Strategy for genetically ablating ACh-evoked DA release from DANs. **f**, Same as **b** for ACh power in control (black; $n = 13$) and $\beta 2$ cKO^{DAN} (blue; $n = 6$) mice during immobility ($P = 0.5$, Student's two-sample t test). **g**, Example DA fluctuations in control and $\beta 2$ cKO^{DAN} mice. **h**, Same as **f** for DA power ($P = 0.2$). **i**, Example DA

(magenta) and ACh (teal) traces from a $\beta 2$ cKO^{DAN} mouse. **j**, Mean DA–ACh cross-correlation during reward (blue), locomotion (green) and immobility (orange) in $\beta 2$ cKO^{DAN} mice. The 95% CI is shown in grey. **k**, Pearson's correlation coefficient r between DA and ACh in six $\beta 2$ cKO^{DAN} mice normalized to control mice during reward ($P = 0.6$), locomotion ($P = 0.9$) and immobility ($P = 0.4$; all compared with control, Student's two-sample t test). **l**, Peak-normalized DA fluorescence in $\beta 2$ cKO^{DAN} mice versus the phase of periodic ACh fluctuations in the band at 0.5–4 Hz. **m**, Same as **b** for DA power following intra-striatal infusion of saline or the nAChR antagonist DH β E ($P = 0.5$, Student's paired t test; $n = 8$ mice). Group means (\pm s.e.m.) in **b**, **d**, **f**, **h**, **k**, **m** are shown in black. Shaded areas in **b**, **d**, **f**, **h**, **j**, **m** depict s.e.m.

To investigate whether DA locally entrains ACh release in vivo, we simultaneously imaged DA and ACh in the DLS before and after locally infusing a control saline solution or a cocktail of DA receptor antagonists ($n = 4$ mice; Fig. 3a). Within a few minutes of infusion, the latter effectively prevented the rDA1m sensor from reporting spontaneous and reward-evoked changes in extracellular DA levels (Fig. 3b and Extended Data Fig. 7a), confirming our ability to block DA receptor signalling in the area imaged by our optic fibre. By contrast, this manipulation did not alter the timing or magnitude of spontaneous or reward-evoked ACh fluctuations compared with saline-infused mice (Fig. 3c,d and Extended Data Fig. 7b–d). To further test whether DA or other transmitters co-released by DANs (for example, glutamate²⁹ or GABA (γ -aminobutyric acid)³⁰) entrain ACh, we imaged ACh3.0 in the DLS before and after lesioning midbrain DANs with either 6-OHDA ($n = 7$ mice) or viral expression of the pro-apoptotic enzyme caspase-3 ($n = 4$ mice; Extended Data Fig. 7e,f). Spontaneous fluctuations in ACh persisted (Extended Data Fig. 7g,h) and even increased in amplitude and frequency (Extended Data Fig. 7i,j) in chronically lesioned mice, confirming that midbrain DANs are not required for striatal ACh levels to fluctuate periodically during immobility.

Next, we investigated whether ACh might directly entrain DA release within the striatum. We generated mice in which CINs cannot directly evoke axonal release of DA by conditionally deleting the $\beta 2$ nAChR subunit specifically in DANs (*Dat*^{Cre}; $\beta 2$ ^{lox/lox} mice; referred to as $\beta 2$ cKO^{DAN} mice hereafter) and imaged rDA1m and ACh3.0 simultaneously

in the DLS (Fig. 3e). $\beta 2$ cKO^{DAN} mice ($n = 6$) showed intact DA and ACh responses to uncued rewards (Extended Data Fig. 8a,b), in line with the well-established observation that reward-evoked DA release in the striatum derives from somatic bursting of DANs in the midbrain^{3,4}. During immobility, DA and ACh transients were similarly unperturbed, fluctuating periodically at the same rate (Fig. 3f–h) and maintaining their strong coherence and phase relationship (Fig. 3i–l and Extended Data Fig. 8c–e).

To exclude the possibility that homeostatic adaptations were occluding the influence that nAChRs normally exert on DA terminals, we acutely blocked nAChR signalling in the DLS by locally infusing the antagonist DH β E (Extended Data Fig. 8f). Compared with saline, DH β E ($n = 8$ mice) did not significantly affect reward-evoked responses or spontaneous DA and ACh fluctuations (Fig. 3m and Extended Data Fig. 8g–j), nor their coherence and phase relationship (Extended Data Fig. 8k), confirming that the strong coupling between DA and ACh is not dependent on striatal nAChR signalling in vivo.

ACh can also modulate DA release by activating muscarinic M5 receptors on DA axons³¹. Although this mechanism has not been implicated in ACh-evoked DA release^{20–23}, we examined its contribution by imaging DA and ACh following local infusion of the mAChR antagonist scopolamine in the DLS. As expected, this manipulation effectively blocked the detection of spontaneous and reward-evoked ACh transients with the ACh3.0 sensor (Extended Data Fig. 8l–n). By contrast, it did not affect reward-evoked DA release and only mildly diminished the power of

spontaneous DA fluctuations in the band at 0.5–4 Hz (Extended Data Fig. 8o,p), confirming the positive modulatory influence of mAChRs on DA release³¹ and indicating that mAChRs are not required to produce periodic fluctuations in DA during immobility. Together, these data show that the periodicity and consistent temporal relationship between DA and ACh transients are not generated locally in the striatum through direct molecular interactions between these neuromodulators.

DA fluctuations arise in the midbrain

Our failure to identify strong intra-striatal interactions between DA and ACh suggests that their coupling may instead be inherited from extra-striatal network dynamics. Previous studies have indicated that phasic DA signals in the striatum arise from midbrain DANs, which fire coherently at 2–4 Hz^{32–34} and integrate inputs distributed throughout the brain³⁵. To determine whether intrinsic rhythms in striatal DA during immobility also originate in the midbrain, we expressed the genetically encoded calcium indicator GCaMP6f in midbrain DANs and simultaneously imaged somatodendritic calcium signals in the SNc and axonal calcium signals in the DLS using fibre photometry (Extended Data Fig. 9a). We observed a strong positive correlation between the two signals during immobility (Extended Data Fig. 9b,c), indicating that spontaneous fluctuations in striatal DA may stem from the somatic activity of DANs in the midbrain. To causally test this, we infused the GABA_A receptor agonist muscimol in the SNc while imaging rDA1m and ACh3.0 in the ipsilateral DLS using photometry (Extended Data Fig. 9d). Muscimol abolished spontaneous DA transients and strongly depressed global levels of DA in the DLS (Extended Data Fig. 9e,f), indicating that intrinsic fluctuations in striatal DA depend on the activity of midbrain DANs. Notably, inhibiting midbrain DANs with muscimol did not diminish spontaneous ACh fluctuations in the striatum (Extended Data Fig. 9e–h), confirming that sub-second transients in striatal DA and ACh are generated separately.

CIN coherence underlies ACh transients

Striatal CINs also fire coherently in response to reward and movement^{5,6,19}, but little is known about the factors that shape intrinsic ACh fluctuations during immobility. To characterize how periodic ACh transients emerge, we recorded the spiking activity of putative CINs (pCINs) from the DLS using high-density multi-shank silicon probes (Extended Data Fig. 10a). We distinguished pCINs, which make up approximately 2% of striatal neurons, by established electrophysiological criteria, including spike waveform, firing rate and discharge properties (Extended Data Fig. 10b–g). pCINs were tonically active (firing rate, 5.7 ± 0.1 spikes per second; $n = 150$ pCINs from 51 recordings in 15 mice) and exhibited irregular, non-bursting firing (Fig. 4a). Notably, their spikes tended to occur synchronously, with 91.7% of pairs of simultaneously recorded pCINs ($n = 157$ pairs) showing a significant peak in their spike cross-correlogram (CCG) at a lag of 0 s (Fig. 4a–c and Extended Data Fig. 10h,i). In addition, 30.6% of pairs showed significant troughs at +0.25 and –0.25 s (Fig. 4c and Extended Data Fig. 10h,i), in line with a 2-Hz rhythm.

To assess whether coordinated pCIN firing accounts for periodic fluctuations in extracellular ACh, we recorded the discharge of pCINs while simultaneously imaging ACh in overlapping regions of the DLS (Fig. 4d). We observed a clear relationship, in which phasic increases in the firing of pCINs preceded peaks in ACh and dips in ACh fluorescence followed coordinated decreases in pCIN firing (Fig. 4e,f and Extended Data Fig. 10j–p). In both cases, fluorescence lagged pCIN firing by ~100 ms, providing an independent estimate of the delay imposed by the kinetics for the ACh3.0 sensor (Extended Data Fig. 2). To determine whether the magnitude of ACh fluctuations correlates with the degree of spike coherence among pCINs, we compared spike-aligned ACh signals during different periods of network synchrony using the

fraction of synchronously active pCINs as a proxy. Spikes occurring during periods of high coherence (that is, when all recorded pCINs were synchronously active) were associated with large ACh transients that gradually declined in amplitude as coherence decreased (Fig. 4g,h). By contrast, spikes occurring in isolation (that is, during periods of low network coherence) did not result in appreciable changes in extracellular ACh levels (Fig. 4g,h). Together, these data strongly suggest that coherent CIN firing drives periodic ACh fluctuations, the amplitude of which reflects the degree of local spike coherence among neighbouring CINs.

Glutamate inputs drive ACh fluctuations

How does coherence among CINs arise? Striatal CINs receive convergent excitatory afferents from distributed cortical and thalamic regions³⁶, which can produce oscillations in the delta range (that is, 1–4 Hz) in non-human primates and rodents during decision-making and different states of arousal, including during quiet wakefulness^{34,37,38}. We therefore postulated that synchronized glutamatergic inputs may coordinate CINs to produce periodic fluctuations in extracellular ACh levels. To test this, we imaged ACh while recording striatal spiking activity and local field potential (LFP) oscillations, which largely reflect the activity of afferent inputs. ACh fluorescence was strongly modulated with respect to LFP oscillations in the frequency band at 0.5–4 Hz (Fig. 4i,k), indicating that coherence among CINs may be imparted by excitatory afferents. Indeed, the vast majority of pCINs recorded (94.6%) were significantly entrained to LFP oscillations at 0.5–4 Hz with a preferred phase of 218 ± 6 degrees (Fig. 4j,k), in line with negative LFP deflections reflecting an increase in excitatory drive onto pCINs. To further test whether glutamatergic inputs drive periodic ACh fluctuations, we delivered a cocktail of ionotropic glutamate receptor (iGluR) blockers locally in the DLS while imaging ACh3.0 and rDA1m (Fig. 4l). This treatment did not significantly decrease global ACh levels compared with saline (Extended Data Fig. 9j), in line with the fact that CINs continue to fire cell autonomously in vivo in the absence of glutamatergic drive³⁹. By contrast, iGluR blockers reversibly depressed spontaneous ACh transients (Fig. 4m,n), but did not significantly depress intrinsic DA fluctuation or global DA levels (Fig. 4o and Extended Data Fig. 9k). Collectively, these data show that periodic fluctuations in DA and ACh are driven, respectively, by extra-striatal dopaminergic and glutamatergic inputs.

Discussion

It is commonly assumed that striatal circuits bathe in a steady concentration of DA and ACh provided by the tonic, cell-autonomous pacing of midbrain DANs and striatal CINs. This neuromodulatory ‘soup’ is occasionally interrupted by phasic increases or decreases in extracellular DA and ACh levels driven by sensory and motor stimuli that have important roles in reinforcement learning and motor performance^{11,14,15}. Here we show that these phasic signals are also prevalent when mice are immobile and in the absence of salient stimuli, with striatal DA and ACh levels fluctuating periodically at approximately 2 Hz. This observation, which hinges on the recent development of fast and specific sensors for DA and ACh with signal-to-noise ratios sufficient to resolve single-trial responses, calls into question the concept of a stable basal neuromodulatory tone in the striatum. Notably, spontaneous changes in DA and ACh do not occur randomly: they are locally coherent at 0.5–4 Hz, with DA signals maintaining a 90-degree phase shift relative to ACh across behavioural states. Thus, although the amplitude of DA and ACh fluctuations varies with behaviour, ACh is unlikely to serve as a simple, context-specific gate or coincidence signal that disambiguates DA transients meant to promote learning versus movement^{9,10}. In addition, this finding suggests that rewards and other salient stimuli do not create unique neuromodulator interactions in the

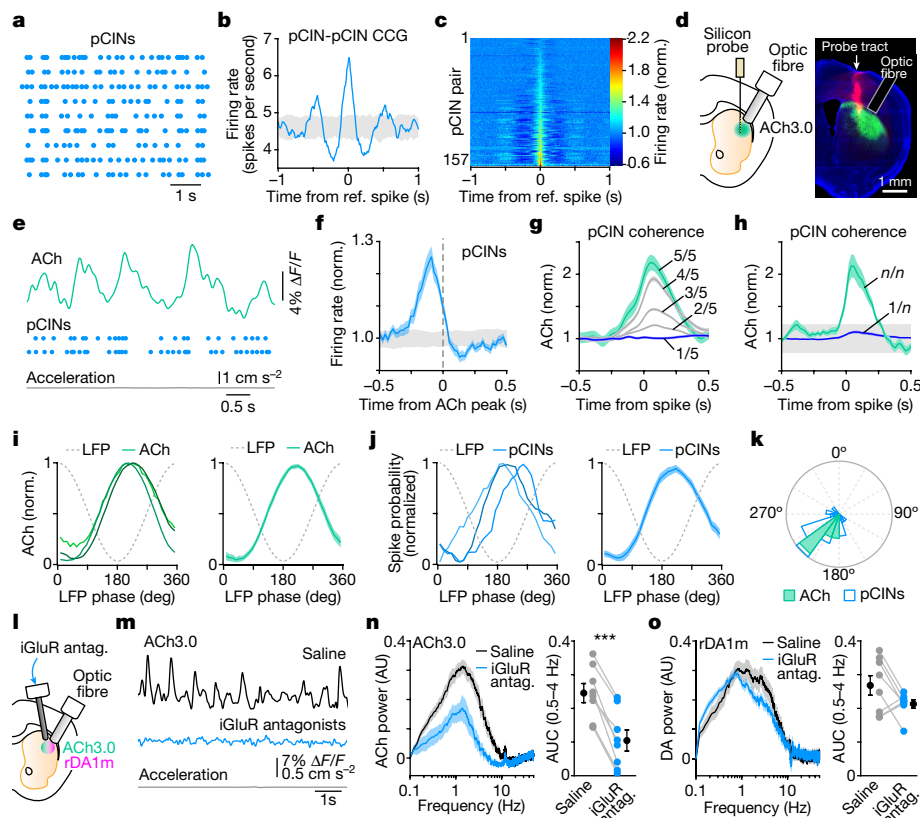


Fig. 4 | Glutamatergic inputs synchronize CIN spiking and drive periodic ACh fluctuations. **a**, Spike raster of nine pCINs recorded simultaneously in the DLS during immobility. **b**, Spike CCG for correlation between a pair of units in **a**. **c**, Heat map of spike cross-correlation for all pCIN pairs ($n = 157$) normalized to the mean firing rate during immobility. **d**, Experimental configuration (left) and representative coronal section from four similar mice showing the silicon probe track (red) near the optic fibre used to image ACh3.0 (right). **e**, Example simultaneous recording of ACh levels (teal) and spiking from two pCINs (blue) during immobility. **f**, Average pCIN firing rate (mean normalized) aligned to peaks in ACh3.0 fluorescence ($n = 22$ units). **g**, Example pCIN spike-aligned ACh signal stratified on the basis of the fraction of concurrently recorded pCINs that were co-active. **h**, Mean pCIN spike-aligned ACh3.0 fluorescence when

only one (blue) or all (teal) concurrently recorded pCINs were co-active. **i**, Three examples of (left) and average ($n = 4$ mice; right) peak-normalized ACh signal aligned to the phase of striatal LFP oscillations in the band at 0.5–4 Hz. **j**, Same as **i** for spike probability in 52 of 55 pCINs (94.5%) that showed a significant phase relationship to LFP at 0.5–4 Hz. **k**, Polar plot of the preferred phase of individual pCINs (blue) and ACh recordings (teal) relative to the LFP at 0.5–4 Hz. **l**, Experimental configuration. **m**, Example ACh fluctuations during immobility following intra-striatal infusion of saline (black) or iGluR antagonists (blue). **n**, Mean ACh power spectrum (left) and AUC in the band at 0.5–4 Hz (right; $P = 2.2 \times 10^{-5}$, Student's paired t test; $n = 8$ mice) during immobility. **o**, Same as **n** for DA ($P = 0.10$). The 95% CI in **b, f, h** is shown in grey. Shaded areas in **f–j, n, o** depict s.e.m.

striatum, but instead engage a common, existing neural architecture that intrinsically supports rhythms in DA and ACh.

Unexpectedly, the rapid, sub-second coordination between DA and ACh does not arise from mutual signalling between CINs and DA axons, despite strong evidence in brain slices that these modulators can directly interact with one another^{20–25}. It is possible that CINs in vivo do not readily drive action potentials in DA axons given the propensity for nAChRs to desensitize in the sustained presence of ACh⁴⁰. Another possibility is that DA and ACh release in vivo is not as synchronous as the electrical and optogenetic stimulations required to evoke DA release *ex vivo*^{21–23}. Notably, our data do not rule out more subtle intra-striatal interactions between DA and ACh that are context dependent²⁰, that take place on subcellular scales not resolved by photometry or that develop on time courses slower than those investigated here. Indeed, the reinforcing properties of nicotine depend on nAChR signalling onto midbrain DANs⁴¹, and prolonged changes in DA receptor signalling are known to alter the electrophysiological properties of striatal CINs^{6,42}.

Our data instead support a model in which spontaneous rhythms in striatal DA and ACh are inherited from extra-striatal afferents. Fluctuations in striatal DA reflect the somatic activity of dopaminergic inputs from the ventral midbrain, while ACh transients are driven by glutamatergic afferents acting to synchronize the discharge of

neighbouring CINs. Excitatory inputs from the cortex and thalamus are sufficient to drive phasic elevations in ACh⁴³ and may contribute to pauses in CIN firing through feed-forward inhibition or periodic withdrawal of excitatory drive⁴⁴. Notably, the magnitude of ACh fluctuations correlates with the degree of population synchrony among CINs, which increases when the brain produces concerted movements¹⁹ or responds to salient sensory stimuli⁶. Striatal ACh levels may therefore be construed as a moment-to-moment measure of coherence in the activity of distributed cortico- and thalamostriatal afferents. Midbrain DANs similarly integrate excitatory (and inhibitory) inputs from many brain areas³⁵ and exhibit baseline correlations in spiking that increase in strength following reward presentation and learning³², and their coherent discharge accounts for phasic changes in striatal DA levels more so than bursting of individual neurons³³. Thus, DA and ACh both reflect the concerted dynamics of widely distributed neural circuits⁴⁵. How DA rhythms coordinate with ACh rhythms in the DLS and in other striatal regions, including in the ventral striatum, remains an important question for future investigations, but a fascinating possibility is that midbrain DANs and striatal CINs innervating contiguous striatal regions are embedded in parallel cortico–basal ganglia–thalamocortical loops and sample common inputs oscillating in the range of 0.5–4 Hz^{34,37,38}.

Together, our data provide a new framework for understanding how the basal ganglia motivate and reinforce behaviour. First, the fact that DA and ACh levels fluctuate constantly indicates that the net effect of one modulator on striatal circuits cannot be fully understood without taking into consideration the other, as the striatum is composed of multiple populations of cells expressing G-protein-coupled receptors for both modulators that engage distinct (and sometimes antagonistic) intracellular signalling cascades. Second, the presence of spontaneous reward-like rhythms in DA and ACh indicates that the established functions of both modulators in learning and synaptic plasticity may extend beyond the time of reward delivery. Indeed, learning, decisions and actions are not exclusively driven by external rewards and salient sensory stimuli. Third, the phase offset between DA and ACh may create temporally defined windows for learning, such that synaptic plasticity may preferentially occur when direct- and indirect-pathway SPNs fire within specific phases of this endogenous rhythm^{12,13,46}, with repeated reactivation of SPN ensembles during post-learning rest offering a potential solution to the credit assignment problem⁴⁷. Lastly, intrinsic fluctuations in DA and ACh may help specify the timing of self-paced volitional actions^{7,14,15,19} as well as sustain cognitive processes that lack overt behavioural correlates^{48–50}. Thus, the autonomously coordinated rhythms in DA and ACh found here provide a lens through which to understand the structure of activity in the basal ganglia as well as its impact on behaviour in health and in neuropsychiatric disorders.

Online content

Any methods, additional references, Nature Portfolio reporting summaries, source data, extended data, supplementary information, acknowledgements, peer review information; details of author contributions and competing interests; and statements of data and code availability are available at <https://doi.org/10.1038/s41586-023-05995-9>.

- Schultz, W. Behavioral theories and the neurophysiology of reward. *Annu. Rev. Psychol.* **57**, 87–115 (2006).
- O'Doherty, J. P., Cockburn, J. & Pauli, W. M. Learning, reward, and decision making. *Annu. Rev. Psychol.* **68**, 73–100 (2017).
- Mirenowicz, J. & Schultz, W. Preferential activation of midbrain dopamine neurons by appetitive rather than aversive stimuli. *Nature* **379**, 449–451 (1996).
- Cohen, J. Y., Haesler, S., Vong, L., Lowell, B. B. & Uchida, N. Neuron-type-specific signals for reward and punishment in the ventral tegmental area. *Nature* **482**, 85–88 (2012).
- Morris, G., Arkadir, D., Nevet, A., Vaadia, E. & Bergman, H. Coincident but distinct messages of midbrain dopamine and striatal tonically active neurons. *Neuron* **43**, 133–143 (2004).
- Aosaki, T., Graybiel, A. M. & Kimura, M. Effect of the nigrostriatal dopamine system on acquired neural responses in the striatum of behaving monkeys. *Science* **265**, 412–415 (1994).
- Costa, R. M. A selectionist account of de novo action learning. *Curr. Opin. Neurobiol.* **21**, 579–586 (2011).
- Coddington, L. T. & Dudman, J. T. Learning from action: reconsidering movement signaling in midbrain dopamine neuron activity. *Neuron* **104**, 63–77 (2019).
- Berke, J. D. What does dopamine mean? *Nat. Neurosci.* **21**, 787–793 (2018).
- Klaus, A., Alves da Silva, J. & Costa, R. M. What, if, and when to move: basal ganglia circuits and self-paced action initiation. *Annu. Rev. Neurosci.* **42**, 459–483 (2019).
- Cox, J. & Witten, I. B. Striatal circuits for reward learning and decision-making. *Nat. Rev. Neurosci.* **20**, 482–494 (2019).
- Shen, W. et al. M4 muscarinic receptor signaling ameliorates striatal plasticity deficits in models of L-DOPA-induced dyskinesia. *Neuron* **88**, 762–773 (2015).
- Reynolds, J. N. J. et al. Coincidence of cholinergic pauses, dopaminergic activation and depolarisation of spiny projection neurons drives synaptic plasticity in the striatum. *Nat. Commun.* **13**, 1296 (2022).
- Howe, M. W. & Dombeck, D. A. Rapid signalling in distinct dopaminergic axons during locomotion and reward. *Nature* **535**, 505–510 (2016).
- da Silva, J. A., Tecuapetla, F., Paixao, V. & Costa, R. M. Dopamine neuron activity before action initiation gates and invigorates future movements. *Nature* **554**, 244–248 (2018).
- Panigrahi, B. et al. Dopamine is required for the neural representation and control of movement vigor. *Cell* **162**, 1418–1430 (2015).
- Engelhard, B. et al. Specialized coding of sensory, motor and cognitive variables in VTA dopamine neurons. *Nature* **570**, 509–513 (2019).
- Mohebi, A. et al. Dissociable dopamine dynamics for learning and motivation. *Nature* **570**, 65–70 (2019).
- Howe, M. et al. Coordination of rapid cholinergic and dopaminergic signaling in striatum during spontaneous movement. *eLife* **8**, e44903 (2019).
- Sulzer, D., Cragg, S. J. & Rice, M. E. Striatal dopamine neurotransmission: regulation of release and uptake. *Basal Ganglia* **6**, 123–148 (2016).
- Threlfell, S. et al. Striatal dopamine release is triggered by synchronized activity in cholinergic interneurons. *Neuron* **75**, 58–64 (2012).
- Cachope, R. et al. Selective activation of cholinergic interneurons enhances accumbal phasic dopamine release: setting the tone for reward processing. *Cell Rep.* **2**, 33–41 (2012).
- Liu, C. et al. An action potential initiation mechanism in distal axons for the control of dopamine release. *Science* **375**, 1378–1385 (2022).
- Straub, C., Tritsch, N. X., Hagan, N. A., Gu, C. & Sabatini, B. L. Multiphasic modulation of cholinergic interneurons by nigrostriatal afferents. *J. Neurosci.* **34**, 8557–8569 (2014).
- Chuhma, N., Mingote, S., Moore, H. & Rayport, S. Dopamine neurons control striatal cholinergic neurons via regionally heterogeneous dopamine and glutamate signaling. *Neuron* **81**, 901–912 (2014).
- Sun, F. et al. Next-generation GRAB sensors for monitoring dopaminergic activity in vivo. *Nat. Methods* **17**, 1156–1166 (2020).
- Jing, M. et al. An optimized acetylcholine sensor for monitoring in vivo cholinergic activity. *Nat. Methods* **17**, 1139–1146 (2020).
- Tritsch, N. X. & Sabatini, B. L. Dopaminergic modulation of synaptic transmission in cortex and striatum. *Neuron* **76**, 33–50 (2012).
- Hnasko, T. S. et al. Vesicular glutamate transport promotes dopamine storage and glutamate corelease in vivo. *Neuron* **65**, 643–656 (2010).
- Tritsch, N. X., Ding, J. B. & Sabatini, B. L. Dopaminergic neurons inhibit striatal output through non-canonical release of GABA. *Nature* **490**, 262–266 (2012).
- Shin, J. H., Adrover, M. F., Wess, J. & Alvarez, V. A. Muscarinic regulation of dopamine and glutamate transmission in the nucleus accumbens. *Proc. Natl Acad. Sci. USA* **112**, 8124–8129 (2015).
- Joshua, M. et al. Synchronization of midbrain dopaminergic neurons is enhanced by rewarding events. *Neuron* **62**, 695–704 (2009).
- Liu, C., Goel, P. & Kaeser, P. S. Spatial and temporal scales of dopamine transmission. *Nat. Rev. Neurosci.* **22**, 345–358 (2021).
- Fujisawa, S. & Buzsaki, G. A 4 Hz oscillation adaptively synchronizes prefrontal, VTA, and hippocampal activities. *Neuron* **72**, 153–165 (2011).
- Watabe-Uchida, M., Zhu, L., Ogawa, S. K., Vamanrao, A. & Uchida, N. Whole-brain mapping of direct inputs to midbrain dopamine neurons. *Neuron* **74**, 858–873 (2012).
- Guo, Q. et al. Whole-brain mapping of inputs to projection neurons and cholinergic interneurons in the dorsal striatum. *PLoS ONE* **10**, e0123381 (2015).
- Neske, G. T. Sleepy circuits in vigilant mice? A slow cortical oscillation occurring during multiple arousal states. *J. Neurosci.* **37**, 7294–7296 (2017).
- Nacher, V., Ledberg, A., Deco, G. & Romo, R. Coherent delta-band oscillations between cortical areas correlate with decision making. *Proc. Natl Acad. Sci. USA* **110**, 15085–15090 (2013).
- Lee, K. et al. Gain modulation by corticostriatal and thalamostriatal input signals during reward-conditioned behavior. *Cell Rep.* **29**, 2438–2449 (2019).
- Quick, M. W. & Lester, R. A. Desensitization of neuronal nicotinic receptors. *J. Neurobiol.* **53**, 457–478 (2002).
- Maskos, U. et al. Nicotine reinforcement and cognition restored by targeted expression of nicotinic receptors. *Nature* **436**, 103–107 (2005).
- Choi, S. J. et al. Alterations in the intrinsic properties of striatal cholinergic interneurons after dopamine lesion and chronic L-DOPA. *eLife* **9**, e56920 (2020).
- Mamaligas, A. A., Barcomb, K. & Ford, C. P. Cholinergic transmission at muscarinic synapses in the striatum is driven equally by cortical and thalamic inputs. *Cell Rep.* **28**, 1003–1014 (2019).
- Zhang, Y. F., Reynolds, J. N. J. & Cragg, S. J. Pauses in cholinergic interneuron activity are driven by excitatory input and delayed rectification, with dopamine modulation. *Neuron* **98**, 918–925 (2018).
- Beeler, J. A. & Kisbye Dreyer, J. Synchronicity: the role of midbrain dopamine in whole-brain coordination. *eNeuro* **6**, ENEURO.0345-18.2019 (2019).
- Shen, W., Flajolet, M., Greengard, P. & Surmeier, D. J. Dichotomous dopaminergic control of striatal synaptic plasticity. *Science* **321**, 848–851 (2008).
- Liu, Y., Mattar, M. G., Behrens, T. E. J., Daw, N. D. & Dolan, R. J. Experience replay is associated with efficient nonlocal learning. *Science* **372**, eabf1357 (2021).
- Graybiel, A. M. The basal ganglia and chunking of action repertoires. *Neurobiol. Learn. Mem.* **70**, 119–136 (1998).
- Soares, S., Atallah, B. V. & Paton, J. J. Midbrain dopamine neurons control judgment of time. *Science* **354**, 1273–1277 (2016).
- Liu, Y., Nour, M. M., Schuck, N. W., Behrens, T. E. J. & Dolan, R. J. Decoding cognition from spontaneous neural activity. *Nat. Rev. Neurosci.* **23**, 204–214 (2022).

Publisher's note Springer Nature remains neutral with regard to jurisdictional claims in published maps and institutional affiliations.

Springer Nature or its licensor (e.g. a society or other partner) holds exclusive rights to this article under a publishing agreement with the author(s) or other rightsholder(s); author self-archiving of the accepted manuscript version of this article is solely governed by the terms of such publishing agreement and applicable law.

© The Author(s), under exclusive licence to Springer Nature Limited 2023

Methods

Ethical compliance

All experimental procedures were performed in accordance with protocols approved by the NYU Langone Health (NYULH) Institutional Animal Care and Use Committee (protocol no. IA16-02082) and in compliance with the Guide for Animal Care and Use of Laboratory Animals.

Animals

Mice were housed in groups before surgery and singly after surgery under standard laboratory conditions ($70 \pm 2^\circ\text{C}$; $50\% \pm 10\%$ humidity; reverse 12-h light/dark cycle, with darkness from 10 a.m. to 10 p.m.) with ad libitum access to food and water, except when they were water restricted to incite consumption of water rewards. For conditional deletion of ChAT from forebrain cholinergic interneurons, a line with *loxP*-flanked *ChAT* was crossed with *Nkx2.1^{Cre}* transgenic mice (both kindly provided by R. Machold, NYULH), as described previously⁵¹. For conditional deletion of the $\beta 2$ subunit of nAChR in DA neurons, a line with *loxP*-flanked $\beta 2$ (ref. 52; kindly provided by M. Crair, Yale University) was crossed with *Dat^{Cre}* knock-in mice⁵³ (Jackson Laboratory, strain no. 006660). C57BL6/J mice were used as control animals (Jackson Laboratory, strain no. 000664). Experiments were carried out using both male and female mice at 8–24 weeks of age (for fibre photometry experiments, 54% of the animals used were female; for electrophysiology experiments, 50% of the animals used were female); we did not observe significant differences between females and males (Extended Data Fig. 3o,p) and therefore used combined data for analyses.

Stereotaxic surgery

Mice were anaesthetized with isoflurane, placed in a stereotaxic apparatus (Kopf Instruments) on a heating blanket (Harvard Apparatus) and administered ketoprofen (10 mg kg^{-1} , subcutaneous). The scalp was shaved and cleaned with ethanol and iodine solutions before exposing the skull. For simultaneous recordings of DA and ACh in the DLS, craniotomies were drilled above the injection site (from bregma, in mm: anteroposterior (AP) +0.5, mediolateral (ML) +2.5 for 0° angle implants or AP +0.5, ML +3.25 for 30° angle implants). Then, 200 nl of a 1:1 mix of AAV9-hSyn-ACh3.0 (titre, 1.46×10^{13} genome copies per mL (GC/mL); Vigene Biosciences) and AAV9-hSyn-rDA1m (titre, 1.91×10^{13} GC/mL; Vigene Biosciences) was injected 2.0 mm below the dura (0° angle) or 1.6 mm below the dura (30° angle) at a rate of 100 nl min^{-1} using a microsyringe pump (KD Scientific, Legato III) fitted with a Hamilton syringe (170IN, gastight $10 \mu\text{l}$) connected to a pulled-glass injection micropipette ($100\text{-}\mu\text{m}$ tip; Drummond Wiretrol II) by polyethylene tubing filled with mineral oil. Injection micropipettes were left in place for 5 min before removal. The optimal dilution of each AAV was empirically determined to enable strong expression while avoiding toxicity. Optic fibres ($400\text{-}\mu\text{m}$ diameter; numerical aperture (NA) = 0.5) were either custom made (an optic fibre (Thorlabs, FP400URT) connected to a ceramic ferrule (Thorlabs, CFLC440)) or purchased from RWD Life Science (R-FOC-BL400C-50NA). Fibres were implanted above the injection site and cemented to the skull using C&B metabond (Parkell). Only fibres with greater than 75% transmission efficiency were selected for surgical implantation. For mice used for simultaneous recording of ACh and DA in the DLS and ipsilateral DMS, additional craniotomies were drilled above the DMS injection site (from bregma, in mm: AP +0.7, ML +1.3 for -5° angle implants). Then, 200 nl of a 1:1 mix of AAV9-hSyn-ACh3.0 and AAV9-hSyn-rDA1m was injected 2.0 mm below the dura and a second optic fibre was implanted at a depth of 1.85 mm below the dura.

For simultaneous recording of GCaMP6^f signal in the DLS and SNc, a craniotomy was drilled above the SNc (from bregma, in mm: AP -3.14, ML +1.42) in *Dat^{Cre}* knock-in mice. Then, 400 nl of AAV1-hSyn-FLEX-GCaMP6f (titre, 4.38×10^{13} ; Penn Vector Core) was injected at a depth of 4.0 mm below the dura at a rate of 100 nl min^{-1} . An optic fibre

cannula was implanted above the injection site, and a second optic fibre cannula was implanted above the DLS (from bregma, in mm: AP +0.5, ML +2.5, at a depth of 2.0 mm); both were cemented to the skull using C&B metabond.

For mice used for acute intra-striatal pharmacological infusions in the DLS, a custom guide cannula (Plastics One; 26 gauge) was chronically implanted ipsilateral to the chronic optic fibre implant at AP +0.5 mm and ML +1.7 mm at a -10° angle and a depth of 1.75 mm below the surface of the pia. For mice used for acute pharmacological infusions in the SNc, a custom guide cannula was chronically implanted at AP -3.14 mm and ML +1.42 mm at a depth of 4.0 mm below the surface of the pia, posterior to the chronic optic fibre implanted in the DLS, as above. Guide cannulas were cemented to the skull using C&B metabond and covered with dummy cannulas. All mice had a custom titanium headpost implanted over lambda using C&B metabond to allow head fixation during recordings. Mice were allowed to recover in their cage for 2 weeks before habituation to head fixation, treadmill and lick spout training, and recordings.

For mice used for acute electrophysiological recordings in the DLS, a second surgery was performed after the post-recovery period, habituation to head fixation and treadmill training. Mice were head-fixed using the previously cemented titanium headpost. A craniotomy centred on ML +2.0 mm and extending from AP -0.5 mm to +1.5 mm was drilled and the dura was carefully removed 24 h before recording. For acute electrophysiological recordings in the DMS, the craniotomy was centred on ML +1.0 mm. A second craniotomy (AP -1.0 mm, ML -1.0 mm) was drilled for grounding during recordings. Both craniotomies were covered with silicone sealant (Kwik-Cast) until recording. After craniotomies, mice were allowed to recover in their cage for 1 day before recordings.

For experiments evaluating the effects of DA neuron loss on entrainment of ACh release, an additional stereotaxic surgery was performed under isoflurane anaesthesia after baseline imaging sessions. Desipramine (25 mg kg^{-1}) and pargyline (5 mg kg^{-1}) were administered intraperitoneally before surgery to increase the selectivity and efficacy of 6-OHDA lesions⁵⁵. A small craniotomy was performed above the SNc ipsilateral to the imaged striatum (AP -3.1 mm, ML +1.3 mm; marked during the first stereotaxic surgery), and $3 \mu\text{g}$ of 6-OHDA (total volume, 200 nl) was injected 4.2 mm below the dura at a rate of 100 nl min^{-1} . Alternatively, DA neurons were lesioned using AAV-mediated Cre-dependent expression of caspase-3 (ref. 56) in the midbrain DA neurons of *Dat^{Cre}* mice. To do so, four craniotomies were performed above the SNc ipsilateral to the imaged striatum (in mm: AP -2.9, ML +0.6; AP -2.9, ML +1.25; AP -3.4, ML +0.6; AP -3.4, ML +1.25; all marked during the first stereotaxic surgery) and 300 nl of AAV1-EF1a-FLEX-taCasp3-TEVp (titre, 2.8×10^{13} GC/mL; UNC Vector Core) was injected at each site 3.8–4.1 mm below the dura at a rate of 100 nl min^{-1} . All mice were allowed to recover in their cage for 2 weeks, with once-daily subcutaneous injections of ketoprofen (10 mg kg^{-1} in 0.9% saline) for the first three postoperative days.

Behaviour analysis

Mice were habituated to head fixation in the rig in a dark soundproof chamber and locomotion on a transparent cylindrical wheel⁵⁷ for a minimum of 5 days before any recording. A subset of mice had access to water within their home cage restricted to incite consumption of water delivered from a spout at semi-random intervals during imaging sessions. Licking was monitored using a capacitive touch sensor (Sparkfun, AT42QT1010). Solenoid valve (Lee Company, LHQA0531220H) opening and lick sensor signals were acquired using Wavesurfer as digital inputs to a National Instruments data acquisition board (PCIe-6353) and breakout terminal block (BNC-2090A) at a sampling rate matching the photometry signal acquisition rate. Reward delivery and lick events exceeding a threshold of 0.5 V were recorded as time points. Analyses and figures of reward-evoked DA and ACh transients were limited to solenoid openings without detected licks in the preceding 0.2 s and with consummatory licks detected within 1 s of solenoid valve opening,

unless specified otherwise. On average, the first lick occurred within 164 ± 12 ms of solenoid opening.

Treadmill velocity was extracted from positional information provided by a rotary encoder (MA3 magnetic shaft encoder, US Digital), downsampled to 50 Hz for all recordings. Immobility was defined as any period of time lasting at least 4 s during which velocity did not exceed 0.25 cm s^{-1} beginning at minimum 0.5 s after the treadmill velocity decreased below 0.25 cm s^{-1} and ending 1 s before the treadmill velocity exceeded 0.25 cm s^{-1} again. Solenoid openings, licking responses and postural adjustments on the wheel (for example, grooming) detected using an infrared camera (Sony AKK CA20 2.8 mm FPV camera) were excluded from periods of immobility. Movement bouts were defined as any period of time when absolute treadmill velocity exceeded 4 cm s^{-1} for a minimum of 4 s, preceded and followed by 4 s of immobility. Treadmill acceleration was calculated as the first derivative of smoothed (movmean function in MATLAB; window, 0.2 s) treadmill velocity. Peaks of positive acceleration were determined by finding the time points of local maxima (findpeaks function in MATLAB with optimized thresholds, minimal prominence: 0.5 cm s^{-2}) during periods of active locomotion.

Open field experiments were conducted in a $30 \times 30 \text{ cm}^2$ arena with a clear plexiglass floor and walls cleaned thoroughly between trials. Mice were habituated to the arena for 30 min per day for a minimum of 5 days before recording. On the day of recording, individual animals were placed in the arena for 30 min while a camera (Basler, acA2000-165um NIR) placed 20 in below the centre of the arena captured frames at 30–60 Hz. Each frame's timestamp was acquired using Wavesurfer to allow for alignment to simultaneously recorded photometry data. Periods of immobility and locomotion were isolated using EthoVision XT 11.5 software (Noldus) whenever the centre of mass of the mouse remained below 0.25 cm s^{-1} or exceeded 4 cm s^{-1} , respectively, for a minimum of four consecutive seconds.

Fibre photometry recording

To excite the GRAB sensors ACh3.0 and rDA1m, we used fibre-coupled LEDs at 470 nm (Thorlabs, M470F3) and 565 nm (Thorlabs, M565F3), respectively. Excitation light was passed through a fibreoptic patch cord (Doric, 400 μm , 0.48 NA) to a fluorescence mini-cube (Doric, FMC5_E1(460-490)_F1(500-540)_E2(555-570)_F2(580-680)_S) and connected to the chronic optic fibre implant in the mouse by a fibreoptic patch cord (Doric, 400 μm , 0.48 NA). Emission light was collected through the same patch cord and fluorescence mini-cube connected to two photoreceivers (Newport, 2151; set to DC mode) using a fibreoptic patch cord (Doric, 600 μm , 0.48 NA); one for green emitted light and another for red emitted light. Excitation light was delivered in one of two modes: continuous wave (CW) or frequency modulated (FM). We used the former to image mice expressing a single sensor and when performing concurrent *in vivo* extracellular recordings to minimize opto-electric artefacts. FM mode was used for imaging DA and ACh sensors simultaneously to minimize cross-talk between the fluorescence channels. In CW mode, light power measured (Thorlabs, PM100D) at the tip of the fibreoptic patch cord was set to 20–60 μW by manually adjusting the LED driver before each recording. In FM mode, a sinusoid generated using Wavesurfer software (Janelia) and output from a National Instruments data acquisition board (PCIe-6353) and breakout terminal block (BNC-2090A) was used to drive the fibre-coupled LED. The 473-nm and 565-nm LEDs were modulated at either 217 Hz or 319 Hz, alternating between recording sessions. Light power was set by adjusting the amplitude and offset parameters of the sinusoidal control voltage by monitoring the output voltage from the photoreceiver using Wavesurfer software, to achieve a sinusoid peak-to-peak amplitude of 1–2 V. After each recording session, light power (18–62 μW) was measured at the tip of the fibreoptic patch cord. We ensured that imaging in FM mode did not generate artefactual oscillations by repeating key observations in mice with only one fluorescent sensor expressed at a

time in CW mode. Photometry signals read out by the photoreceiver were digitized at 2 kHz (for CW mode) or 5 kHz (for FM mode) by a National Instruments acquisition board (NI BNC-2090A) or at 30 kHz (for combined fibre photometry and acute electrophysiology recordings) by an Open Ephys acquisition board.

Acute electrophysiological recording

Electrophysiological recordings were made with silicon microprobes⁵⁸ (128D, IDAX Microelectronics) affixed to metal rods acutely lowered into the brain using a micromanipulator (Scientifica, PatchStar). For DLS recordings, probes were inserted perpendicularly to the brain surface at approximately AP +0.0 to +1.0 mm and ML +2.0 or +2.5 mm to a depth of about 2.5–3.0 mm. Before insertion on each recording day, the electrode shafts were coated with fluorescent dye (Dil; Thermo Fisher Scientific, V22885) for post hoc identification of the probe insertion location. Probes were lowered at a speed of $1 \mu\text{m s}^{-1}$ to limit tissue damage and, once at the desired depth, were left in place for at least 45 min before initiating a recording, to allow for the tissue to settle and minimize unit drift. Electrophysiological data were recorded with Open Ephys at a sampling rate of 30 kHz. Wheel positional encoder and, when applicable, photometry data were also recorded using an I/O board connected to the Open Ephys acquisition board at a sampling rate of 30 kHz.

Fibre photometry analysis

Photometry signal processing. Raw photometry signals collected as a voltage from the photoreceiver were processed using custom MATLAB code. For recordings in CW mode, raw voltage signals were first low-pass filtered at 20 Hz using a Butterworth filter to remove high-frequency noise. The filtered signal was then downsampled to 50 Hz (above the Nyquist frequency to prevent aliasing), and the final photometry signal (output as a percentage) was obtained using the equation $\Delta F/F = (F - F_0)/F_0$, in which F_0 is baseline fluorescence. The latter was computed by interpolating the bottom percentile of fluorescence values measured in 10-second-long sliding windows (0% overlap) along the entire photometry trace. For recordings acquired in FM mode, a copy of each sinusoid generated in Wavesurfer was recorded as a reference signal alongside the modulated green and red fluorescence signals from the photoreceivers. We demodulated fluorescence signals as follows. First, each fluorescence signal was band-pass filtered (reference sinusoid frequency ± 10 Hz; Butterworth; order 6) to isolate the main frequency component. Next, we determined whether the reference and fluorescence sinusoids were in phase or out of phase. If they were in phase, we performed phase-dependent demodulation by (1) subtracting the mean of the reference and fluorescence sinusoids to remove any DC offset, (2) multiplying the reference and fluorescence sinusoids, and (3) low-pass filtering (20 Hz) the resulting signal to extract the demodulated fluorescence. More commonly, however, the reference and fluorescence sinusoids were slightly out of phase. In this case, we used a standard quadrature demodulation method (which calls for phase shifting the reference signal by 90 degrees before multiplying it by the fluorescence sinusoid and then low-pass filtering the resulting signal at 20 Hz) to demodulate the fluorescence signal^{59,60}. The demodulated fluorescence traces were finally downsampled to 50 Hz and baseline adjusted as described above.

Frequency analysis. Analysis of frequency components enriched in the ACh and DA photometry signals was performed on raw, unfiltered, non-demodulated, non-downsampled fluorescence signals from time periods when mice were immobile (unless specified otherwise). We computed the fast Fourier transform of these data using the `fft` function in MATLAB and extracted the single-sided amplitude (power) spectrum across frequency domains spanning 0 to $0.5 \times$ acquisition sampling frequency. Power spectra shown in Fig. 1i,m were normalized by subtracting the power at 100 Hz and dividing by the power at 0.1 Hz.

Article

To isolate power specifically contributed by DA and ACh in Fig. 1j,n (and in all similar figures subsequently), we then subtracted the mean normalized power spectrum of the inert fluorophores tdTomato and GFP, respectively, across the same frequency domains. To compare DA and ACh power statistically across mice and conditions (as in Fig. 1k,o and in similar figures subsequently) we computed the AUC of the power spectra within the frequency band at 0.5–4 Hz.

Cross-correlation analysis. To correlate ACh3.0 and rDA1m fluorescence, we calculated the Pearson cross-correlation coefficient r between the two photometry signals using the `xcorr` function in MATLAB (window, 1 s; bin, 20 ms) after parsing them on the basis of behavioural state (that is, reward, locomotion or immobility). CIs were computed by repeatedly calculating Pearson's r after one of the photometry signals was shifted in time (increment, 1 s; repeats, 100) and then extracting the 2.5th and 97.5th percentiles across the correlation window for each bin to generate a 95% CI. The correlation coefficient r and lag at the maximum absolute deflection were computed and compared across behavioural states and/or cohorts, as shown in Fig. 2b,c. We applied the same process to correlate ACh or DA fluorescence and wheel acceleration, as shown in Extended Data Fig. 4h, and to correlate GCaMP6f fluorescence imaged in the DLS and SNC, as shown in Extended Data Fig. 9c.

Coherence analysis. To quantify how closely DA and ACh fluorescence signals co-varied in time and the relative timing between the two signals, we computed their coherence and extracted the magnitude of the coherence and phase offset, respectively. We performed this over different frequency domains to examine in which frequency band coherence was greatest, as well as over time domains to examine whether the degree of coherence and phase offset between DA and ACh varied between behavioural states. We computed coherence using a custom MATLAB script adapted from code acquired from the Buzsáki laboratory⁶¹ (<https://github.com/buzsakilab/buzcode>). In brief, we calculated the magnitude and phase of the DA–ACh coherogram using a multi-taper estimation with the `chronux` function `cohgramc` (window, 10 s; overlap, 5 s; step, 5; padding, 0). We computed CIs by randomly shifting one of the photometry signals (increment, 1 s; repeats, 100) and extracting the 2.5th and 97.5th percentiles of the magnitude and phase of the resultant coherogram for each repetition to generate a 95% CI. To compare coherence at different frequencies, we averaged coherence magnitude and phase offset across the time dimension, as shown in Fig. 2d,f and in other similar figures. To compare each between behavioural states, we calculated the median coherence magnitude and phase offset within the frequency band at 0.5–4 Hz, as shown in Fig. 2e,g and in other figures like it. Phase offset was only examined if a significant effect of coherence magnitude was observed.

Phase analysis. To estimate instantaneous phase across time, each photometry signal was filtered (0.5–4 Hz; Butterworth; order 3) and the phase angle of the Hilbert transform was extracted using the `hilbert` function in MATLAB. We next extracted the amplitude of the DA and ACh fluorescence signals corresponding to each oscillatory cycle (from –180 to +180 degrees; bin size, 10 degrees) and calculated the mean amplitude within each bin. To highlight the temporal relationship between DA and ACh across behavioural states, we normalized the fluorescence amplitude between 0 and 1 across each full cycle, as shown in Fig. 2j and in other figures like it. We applied the same process to determine the relationship between the phase of ACh or DA fluctuations and wheel acceleration, as shown in Extended Data Fig. 4i,j.

Pharmacological infusion analysis. The effects of intra-striatal drug infusions on ACh and DA fluctuations were assessed by comparing photometry signals immediately preceding and following completion of drug infusion, unless specified otherwise. To measure relative changes in the overall extracellular concentration of DA or ACh in the

striatum, we first estimated the fraction of the voltage recorded by the photoreceiver that specifically reflected extracellular neurotransmitter levels (compared with that contributed by autofluorescence of the brain and photometry system). We term this metric the 'global DA or ACh level' and normalized its dynamic range such that a value of 1 reflected the fluorescence attributed to extracellular DA or ACh under baseline recording conditions and a value of 0 reflected the fluorescence in the presence of pharmacological antagonists for either sensor (D1/2R antagonists for rDA1m and mAChR antagonists for ACh3.0; Extended Data Fig. 9f,i–k). We expressed changes in global DA or ACh levels caused by intra-striatal infusions of pharmacological antagonists by normalizing post-infusion fluorescence to pre-infusion levels.

Acute electrophysiological analysis

Spike sorting and putative cell type determination. Raw electrophysiological data were spike sorted using Kilosort 2 (www.github.com/MouseLand/Kilosort2), and the resulting spike clusters were visualized and manually curated using Phy2 (<https://phy.readthedocs.io/en/latest>). High-quality single units were identified on the basis of the following inclusion criteria: (1) waveform trough to peak amplitude exceeding 80 μ V; (2) a minimum of 500 spikes recorded in a recording session of 5,400 s; (3) waveform peaks preceding waveform troughs; and (4) presence of a clear refractory period, as assessed by considering the length of time that the firing rate of a unit was suppressed following a spike in autocorrelograms (window, 1 s; bin, 1 ms). Units passing these quality criteria were then classified into three putative striatal cell types—putative SPNs (pSPNs), pCINs and a third class of unidentified neurons (others, which probably includes fast-spiking interneurons and other GABAergic interneurons)—using established criteria^{62–67} such as firing rate, coefficient of variation, phasic activity index and spike waveform duration. The firing rate of a unit was calculated as the number of spikes divided by the duration of the recording. The coefficient of variation was defined as the standard deviation of the distribution of inter-spike intervals (ISIs) divided by the mean of the distribution. The index of phasic activity was calculated as the fraction of the recording time containing ISIs longer than 2 s. The waveform duration was calculated as the time between the maximum downward spike deflection and the following upward peak. For analyses during immobility or locomotion, we extracted spikes that occurred in windows of time when the animal was determined to be immobile or actively locomoting, respectively, using criteria described in 'Behaviour analysis' above.

Spike train cross-correlation. In recordings with ≥ 2 simultaneously recorded pCINs, we first generated pairs using the `nchoosek` function in MATLAB. For each pair of pCINs, one was randomly selected to be the reference unit and we calculated the spike cross-correlation for that pair as the number of spikes emitted by one pCIN relative to the spikes of the reference unit (window, 2 s; bin, 10 ms). We normalized spike counts to a firing rate by dividing the number of spikes in each time bin by the total number of reference unit spikes and by bin size: firing rate = (spike count/ n_{ref})/bin duration (s). To allow comparisons across units with different baseline firing rates, we mean normalized instantaneous firing rates by subtracting the mean firing rate (μ) of the non-reference unit in a given behavioural state before dividing the resultant value by the same mean: normalized instantaneous rate = (instantaneous rate – μ)/ μ . To compute CIs, we ran a CCG using the same reference unit and a shuffled spike train of the second pCIN. Each shuffled spike train was generated following random permutations of a unit's ISIs before computing the 2.5th and 97.5th percentiles of the resulting shuffled CCGs. Lastly, to assess the proportion of units that significantly increased their firing rate, we identified all the time bins at various lags in which the CCG output was either above or below the 95% CI.

Firing rate change at event times. For recordings in which ACh fluorescence was imaged concurrently with spiking activity, we determined

the instantaneous firing rate of pCINs relative to peaks and troughs in ACh by filtering photometry signals (0.5–4 Hz; Butterworth; order 3), identifying transients larger than 2 s.d. from the filtered signal and computing a peri-event time histogram by aligning spike times to event times such as ACh peaks and ACh troughs. Spike times were counted in 20-ms bins (determined on the basis of the final sampling rate of the photometry signal, 50 Hz) across a 2-s time window centred on the event times and then averaged across all events to generate a rate. We normalized the firing rate change at event times to the mean firing rate for a given behavioural state to allow for comparison between units with different firing rates. To obtain a 95% CI, a shuffled spike train (maintaining the same distribution of ISIs) was instead aligned to event times. To assess the proportion of units that significantly changed their firing rate, we determined the number of bins in which a unit's firing rate either exceeded or fell below the 95% CI.

Coherent spiking analysis. Only recordings with ≥ 2 pCINs and concurrent imaging of ACh fluorescence were included. Spike trains were first parsed to include only spikes occurring during immobility, as defined in 'Behavioural analysis'. For each spike of a selected reference pCIN, we determined whether other pCINs discharged within ± 10 ms by generating peri-event counts relative to spikes. The resulting output was a matrix of binary values, with the number of columns reflecting the length of the spike train of the reference unit and the number of rows corresponding to the number of concurrently recorded units (n). This output matrix was then summed across all rows, such that the range of values of the final vector would be 1 to n . Lastly, the spike times of the reference unit were stratified on the basis of the value within each bin. Bins in which only one of n units spiked reflected low synchrony among the population of pCINs, whereas bins with a value of n out of n possible units corresponded to synchronous activity across all concurrently recorded pCINs. Simultaneously recorded ACh photometry signal was aligned to the stratified spike times of the reference unit, and a spike-triggered average was computed by averaging the photometry signal across each group ($1/n$ to n/n), as shown in Fig. 4g. To compare units across multiple recordings with a variable total number of pCINs, only $1/n$ and n/n spike-triggered averages were used, as shown in Fig. 4h. For computation of a 95% CI, the simultaneously recorded photometry signal was aligned to the spike times in a shuffled spike train (maintaining the same distribution of ISIs) and the 2.5th and 97.5th percentiles were extracted across spike-triggered averages.

LFP analysis. LFP signals were extracted from wideband electrophysiological recordings in one striatal channel and downsampled to 1,250 Hz. The LFP was then filtered at 0.5–4 Hz, and the instantaneous phase was determined using a Hilbert transform. Phase locking was determined by calculating the instantaneous phase angle at each spike time for a given unit during immobility. A histogram of phase angles was calculated, and the circular mean and resultant vector were calculated for each unit, as shown in Fig. 4j. Only units that were significantly modulated (Rayleigh test) were included in the analysis. For recordings where ACh fluorescence was imaged concurrently, phase locking was determined by calculating a histogram of photometry signal amplitude at each phase angle and rescaling across each cycle, as shown in Fig. 4i. Cross-correlation between the filtered LFP signal and concurrently recorded photometry signal was calculated as above.

Histology

Mice were deeply anaesthetized with isoflurane and perfused transcardially with 4% paraformaldehyde in 0.1 M sodium phosphate buffer. Brains were post-fixed for 1–3 days and sectioned coronally (50–100 μ m in thickness) using a vibratome (Leica, VT1000S). ACh3.0 and rDA1m were either imaged directly (that is, endogenous fluorescence; as in Fig. 4d and Extended Data Fig. 1a) or after immunofluorescence staining (Extended Data Figs. 1b–d and 7h) by incubating free-floating sections

with chicken anti-GFP (Abcam, ab13970; 1:2,000) and rabbit anti-DsRed (Takara, 632496; 1:1,000) polyclonal antibodies overnight at 4 °C. DA axons in Extended Data Fig. 7h were labelled using a rat anti-DAT monoclonal antibody (Sigma, MAB369; 1:1,000). The following secondary antibodies (all from Thermo Fisher Scientific) were applied for 2 h at room temperature: goat anti-chicken Alexa Fluor 488 (A-11039; 1:1,000), goat anti-rabbit Alexa Fluor 568 (A-11036; 1:1,000) and goat anti-rat Alexa Fluor 647 (A-21247; 1:1,000). Brain sections were subsequently mounted on superfrost slides and coverslipped with ProLong antifade reagent with DAPI (Molecular Probes). Low-magnification images of whole sections were obtained with an Olympus VS120 slide scanning microscope, and high-magnification optical sections were imaged using a Zeiss LSM 800 Airyscan confocal microscope.

Reagents

Drugs (all from Tocris) were reconstituted and stored according to the manufacturer's recommendations. For systemic antagonism of mAChRs and D2Rs in Fig. 1h–o, scopolamine (2 mg kg⁻¹) and sulpiride (30 mg kg⁻¹) were prepared daily in sterile physiological saline (0.9% NaCl) and administered intraperitoneally 30 min before the start of photometry recordings. For local injections within the DLS, an internal cannula (Plastic One, 33 gauge) was connected to a syringe (Hamilton, 1701N, gastight 10 μ l) through a tube containing either HEPES-buffered sterile saline or a pharmacological agent dissolved in saline and was inserted into the guide cannula before the recording session. Drug infusion controlled by a microsyringe pump (KD Scientific, Legato 111; rate, 50–100 nl min⁻¹) was initiated 10–20 min after baseline recording. The following drugs were used: 1 mM NBQX (2,3-dioxo-6-nitro-1,2,3,4-tetrahydrobenzo[*f*]quinoxaline-7-sulfonamide) and 5 mM D-AP5 (D-(–)-2-amino-5-phosphonopentanoic acid) to block iGluRs, 0.4 mM SCH23390 to block D1Rs, 0.6 mM sulpiride to block D2Rs, 5 mM DH β E (dihydro- β -erythroidine hydrobromide) to block nAChRs and 1 mM scopolamine to block mAChRs. To estimate the extent of drug infusion in the striatum in Fig. 3a, drugs were substituted with Alexa Fluor 594 hydrazide (Invitrogen, A10442). To inhibit neural activity in the ventral midbrain in Extended Data Fig. 9d–h, 1 mM muscimol dissolved in HEPES-buffered sterile saline was infused at a rate of 50 nl min⁻¹ into the SNC.

Statistics

The experiments were not randomized, as comparisons were either made within subjects (for example, saline versus antagonist infusions in the same animal) or between mice of different genotype (for example, control versus $\beta 2$ cKO^{DAN} mice). Data were not acquired with blinding to experimental condition, but were subjected to identical analyses and compared statistically in MATLAB using the following tests (as indicated in the text): Student's paired two-sided *t* test for comparisons between paired data points, Student's two-sample two-sided *t* test for comparisons between unpaired data points and one-way balanced ANOVA followed by Dunn's multiple-comparison test for comparisons among multiple groups. For fibre photometry experiments, n values represent the number of mice. All imaging sessions obtained per condition from the same mouse (average of 2 sessions per condition per mouse; range, 1–4) were concatenated and analysed as $n = 1$. For electrophysiology recordings, n represents the number of units or unit pairs. Histological analyses were independently replicated in at minimum three mice. No statistical methods were used to predetermine sample size. Data are reported in the text and figures as mean \pm s.e.m., with shaded areas and error bars in figures representing s.e.m. Exact *P* values are provided in the text and figure legends, and statistical significance in figures is presented as **P* < 0.05, ***P* < 0.01 and ****P* < 0.001.

Reporting summary

Further information on research design is available in the Nature Portfolio Reporting Summary linked to this article.

Data availability

The data that support the findings of this study are available from the corresponding author on reasonable request. Source data are provided with this paper.

Code availability

All code related to this study was developed in MATLAB and is available at https://github.com/ackrok/Krok-etal_2023.

51. Patel, J. C., Rossignol, E., Rice, M. E. & Machold, R. P. Opposing regulation of dopaminergic activity and exploratory motor behavior by forebrain and brainstem cholinergic circuits. *Nat. Commun.* **3**, 1172 (2012).
52. Burbridge, T. J. et al. Visual circuit development requires patterned activity mediated by retinal acetylcholine receptors. *Neuron* **84**, 1049–1064 (2014).
53. Backman, C. M. et al. Characterization of a mouse strain expressing Cre recombinase from the 3' untranslated region of the dopamine transporter locus. *Genesis* **44**, 383–390 (2006).
54. Chen, T. W. et al. Ultrasensitive fluorescent proteins for imaging neuronal activity. *Nature* **499**, 295–300 (2013).
55. Thiele, S. L., Warre, R. & Nash, J. E. Development of a unilaterally-lesioned 6-OHDA mouse model of Parkinson's disease. *J. Vis. Exp.* <https://doi.org/10.3791/3234> (2012).
56. Yang, C. F. et al. Sexually dimorphic neurons in the ventromedial hypothalamus govern mating in both sexes and aggression in males. *Cell* **153**, 896–909 (2013).
57. Warren, R. A. et al. A rapid whisker-based decision underlying skilled locomotion in mice. *eLife* **10**, e63596 (2021).
58. Yang, L., Lee, K., Villagrancia, J. & Masmanidis, S. C. Open source silicon microprobes for high throughput neural recording. *J. Neural Eng.* **17**, 016036 (2020).
59. Stanford Research Systems. About lock-in amplifiers. <https://www.thinksrs.com/downloads/pdfs/applicationnotes/AboutLIAs.pdf> (2016).
60. Balakrishnan, H. & Verghese, G. Modulation and demodulation. <http://web.mit.edu/6.02/www/s2012/handouts/14.pdf> (2012).
61. Zutshi, I., Valero, M., Fernandez-Ruiz, A. & Buzsaki, G. Extrinsic control and intrinsic computation in the hippocampal CA1 circuit. *Neuron* **110**, 658–673 (2022).
62. Berke, J. D., Okatan, M., Skurski, J. & Eichenbaum, H. B. Oscillatory entrainment of striatal neurons in freely moving rats. *Neuron* **43**, 883–896 (2004).
63. Schmitzer-Torbert, N. C. & Redish, A. D. Task-dependent encoding of space and events by striatal neurons is dependent on neural subtype. *Neuroscience* **153**, 349–360 (2008).
64. Sharott, A., Doig, N. M., Mallet, N. & Magill, P. J. Relationships between the firing of identified striatal interneurons and spontaneous and driven cortical activities in vivo. *J. Neurosci.* **32**, 13221–13236 (2012).
65. Yamin, H. G., Stern, E. A. & Cohen, D. Parallel processing of environmental recognition and locomotion in the mouse striatum. *J. Neurosci.* **33**, 473–484 (2013).
66. Peters, A. J., Fabre, J. M. J., Steinmetz, N. A., Harris, K. D. & Carandini, M. Striatal activity topographically reflects cortical activity. *Nature* **591**, 420–425 (2021).
67. Gage, G. J., Stoetzner, C. R., Wiltschko, A. B. & Berke, J. D. Selective activation of striatal fast-spiking interneurons during choice execution. *Neuron* **67**, 466–479 (2010).

Acknowledgements We thank G. Buzsaki, M. Long, S. Shoham, R. Tsien and members of the Tritsch laboratory for comments on the manuscript and M. Crair (Yale University) and R. Machold (NYULH) for providing the $\beta 2^{flax}$ and $ChAT^{flax};Nkx2.1^{Cre}$ mice, respectively. This work was supported by the National Institutes of Health (DP2NS105553 and R01MH130658 to N.X.T.; T32NS086750, T32GM007308 and T32GM136573 to A.C.K.), the Paolo and Marlene Fresco, Alfred P. Sloan, Dana, Whitehall and Feldstein Medical foundations to N.X.T. and a Vilcek Scholars Award to A.C.K. We acknowledge the New York University Langone Health Rodent Genetic Engineering Laboratory for rederivation, the Genotyping Core Laboratory for mouse genotyping, the Department of Comparative Medicine for animal care and maintenance, and the Neuroscience Institute's imaging facilities for microscope availability. We apologize to those whose work we were unable to cite due to length limits.

Author contributions A.C.K. and N.X.T. conceived of the project, designed and performed experiments, analysed and interpreted the data, and wrote the manuscript. A.C.K. and P.M. wrote code for photometry data acquisition and analyses, M.M. performed DA neuron lesions and helped with photometry data collection and analyses, and X.M. and Y.L. performed experiments to determine the kinetics of ACh3.0 and provided the GRAB sensors rDA1m and ACh3.0.

Competing interests Y.L. is listed as an inventor on a patent application (PCT/CN2018/107533) describing GRAB probes. The other authors declare no competing interests.

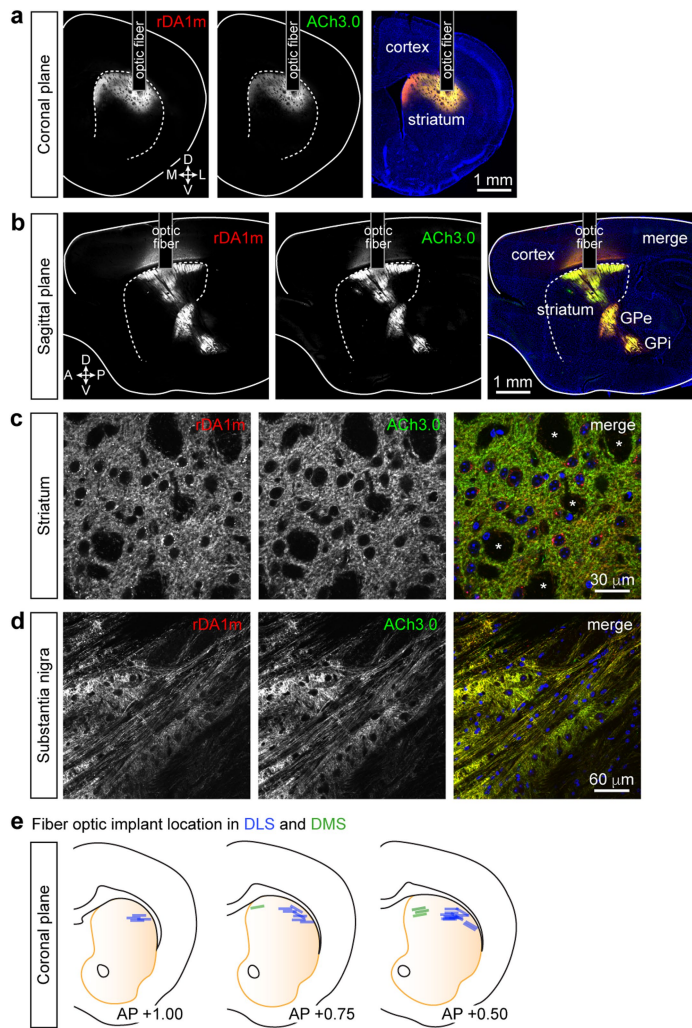
Additional information

Supplementary information The online version contains supplementary material available at <https://doi.org/10.1038/s41586-023-05995-9>.

Correspondence and requests for materials should be addressed to Nicolas X. Tritsch.

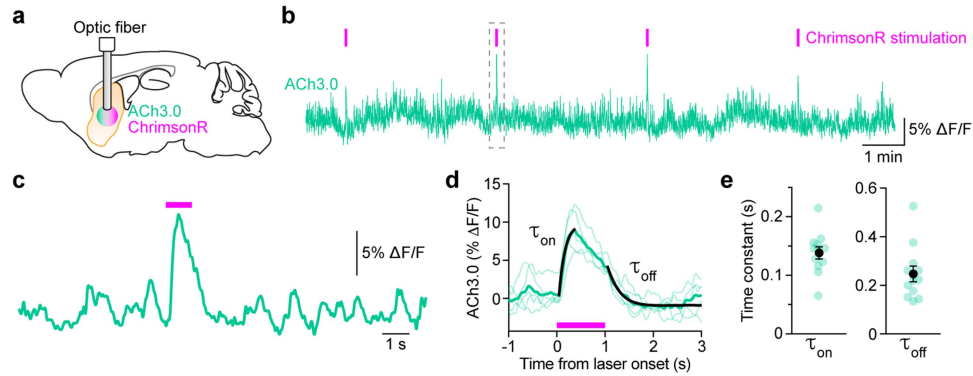
Peer review information Nature thanks Anna Beyeler, Sean Ostlund and the other, anonymous, reviewer(s) for their contribution to the peer review of this work. Peer reviewer reports are available.

Reprints and permissions information is available at <http://www.nature.com/reprints>.



Extended Data Fig. 1 | Characterization of rDA1m and ACh3.0 expression.

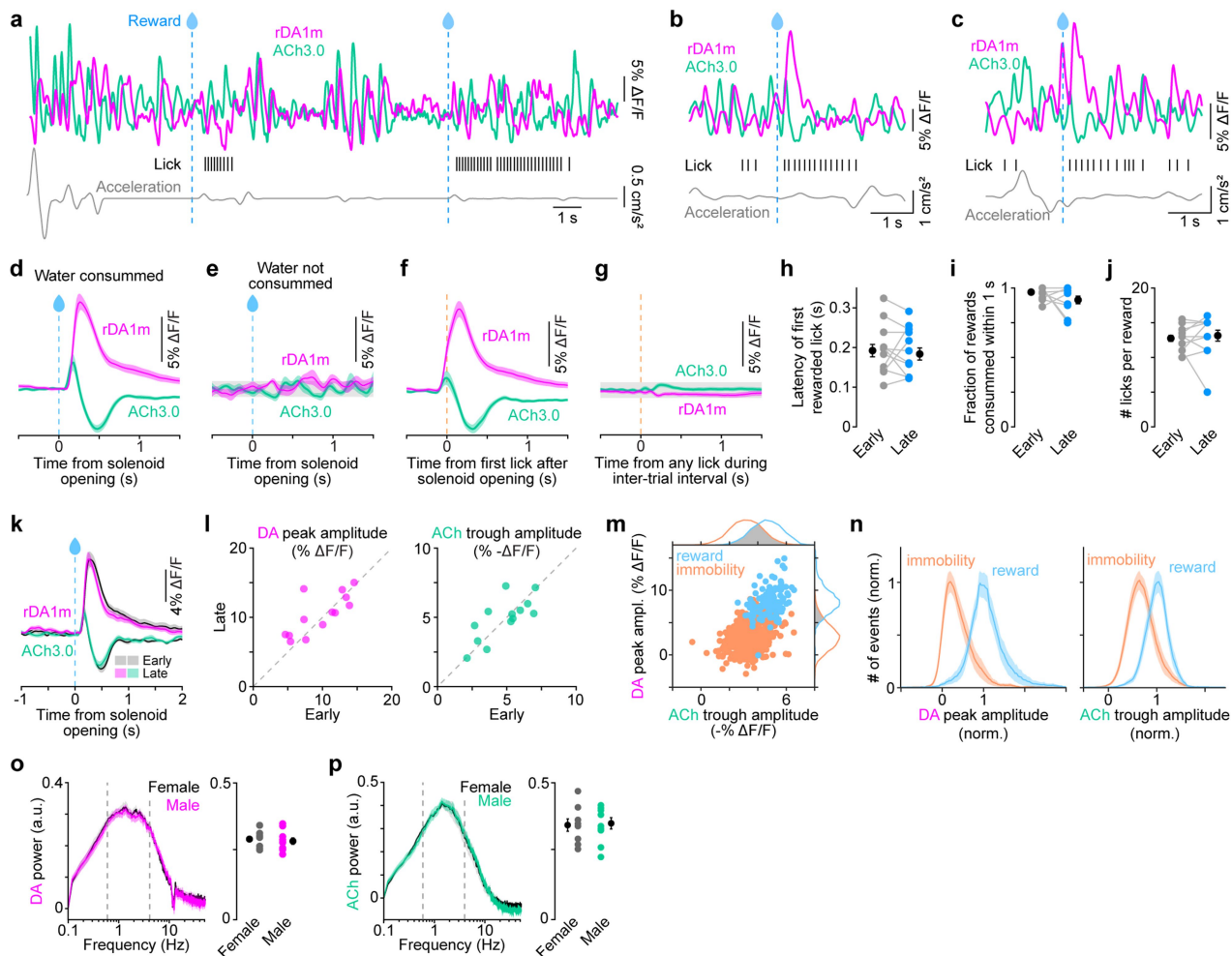
a, Epifluorescence images of endogenous rDA1m (*left*) and ACh3.0 (*middle*) fluorescence in a coronal section of the striatum. *Right*, merged image overlaid with DAPI nuclear stain (blue). Similar results were obtained in $n = 16$ other brains recovered for post-hoc validation of GRAB sensor expression and fiber optic placement. **b**, Epifluorescence images of immuno-enhanced rDA1m and ACh3.0 expressed in the dorsal striatum. Note the presence of rDA1m- and ACh3.0-positive axonal projections in the globus pallidus externus (GPe) and internus (GPi), consistent with the subcellular distribution of dopamine and muscarinic receptors in both direct and indirect-pathway SPNs. **c**, High magnification confocal images (single optical plane) of immuno-enhanced rDA1m and ACh3.0 in a coronal striatal section. Note the localization of both sensors to the somatic membranes of striatal neurons and throughout the neuropil, and their exclusion from corticofugal axon bundles (asterisks). Note also that some rDA1m forms intracellular aggregates. **d**, Same as **c** for a sagittal section of the substantia nigra pars reticulata. Subcellular localization of immuno-enhanced rDA1m and ACh3.0 by high magnification confocal microscopy was independently confirmed in four mice. **e**, Schematic showing the tip of all recovered fiber optic implants in the DLS (blue) and DMS (green) at 3 different anterior-posterior levels relative to bregma (in mm).



Extended Data Fig. 2 | Kinetics of ACh3.0 sensor in the striatum in vivo.

a, Experimental preparation to optogenetically evoke ACh release in vivo using ChrimsonR while simultaneously monitoring ACh levels with ACh3.0 photometry via the same fibre optic. ChrimsonR and ACh3.0 were both virally-expressed. **b**, Example ACh3.0 recording (teal). ChrimsonR was stimulated every 200 s with 635 nm light flashes (20 Hz, 1 s; shown in magenta). **c**, detail of dashed box

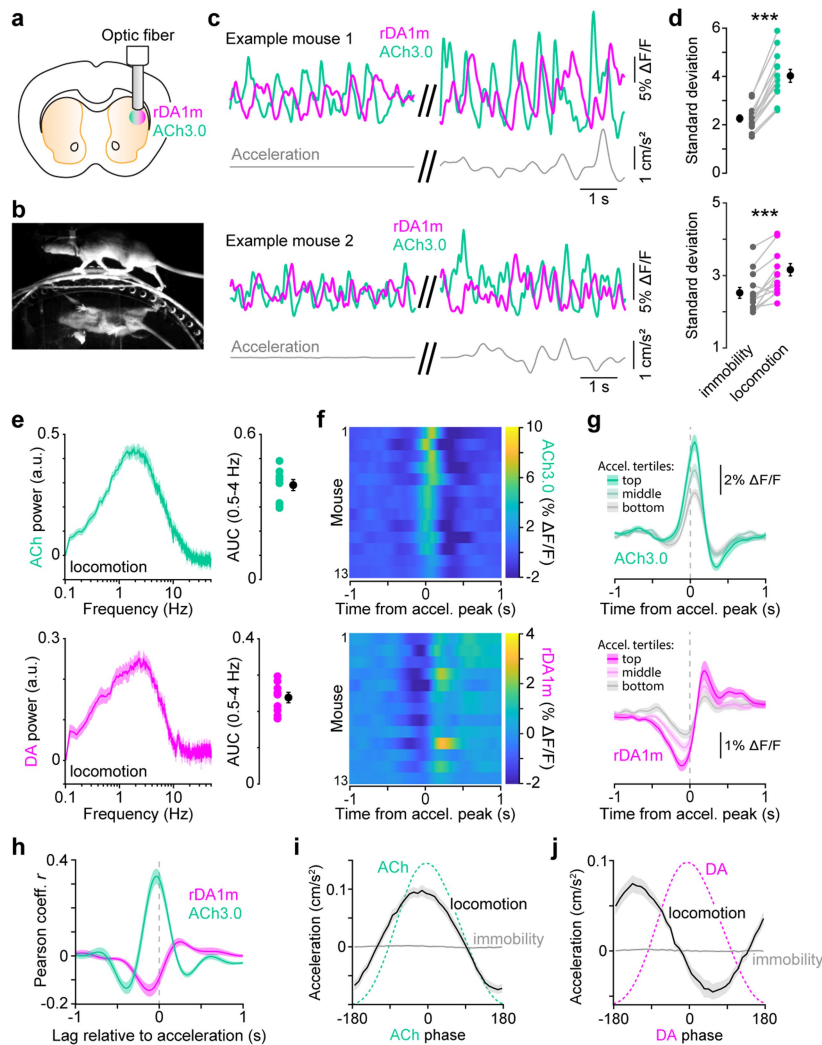
in **b** showing ChrimsonR-evoked ACh release. **d**, Overlay of individual ACh3.0 transients (light teal) from **b** aligned to optogenetic stimulation onset. Group mean shown in dark teal with overlaid exponential fits used to calculate onset (τ_{on}) and offset (τ_{off}) time constants in black. **e**, ACh3.0 τ_{on} (left) and τ_{off} (right). Mean (\pm s.e.m.) shown in black (τ_{on} : 138 ± 10 ms; τ_{off} : 247 ± 32 ms; $n = 12$ trials from 3 mice).



Extended Data Fig. 3 | Reward-evoked DA and ACh responses in the DLS.

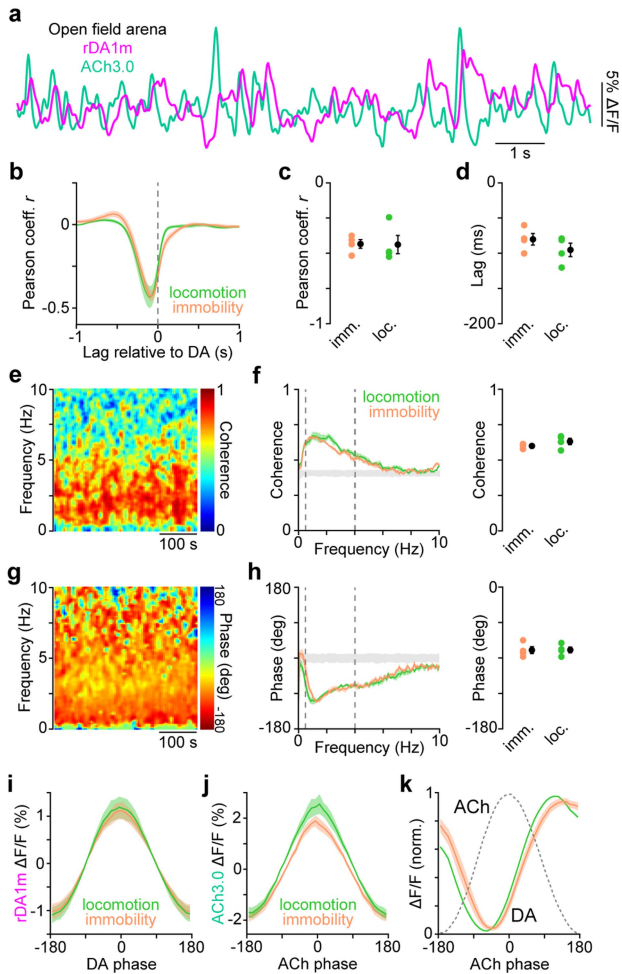
a, Example continuous recording of rDA1m (magenta) and ACh3.0 (teal) fluorescence, lick events (black) and treadmill acceleration (gray) illustrating the temporal dynamics of both sensors. Dashed blue lines depict uncued solenoid valve opening, which in this example did not generate large DA and ACh reward transients. **b**, Other reward response from same mouse. **c**, Example DA and ACh reward responses for a different mouse. **d**, Mean rDA1m (magenta) and ACh3.0 (teal) fluorescence aligned to solenoid valve opening for all uncued water deliveries followed within 1 s by consummatory licking ($n = 13$ mice). **e**, Same as **d** for water deliveries not followed by consummatory licking. Gray: 95% confidence interval. **f**, Same as **d**, but aligned to first lick after solenoid valve opening (i.e., first rewarded lick). **g**, Mean rDA1m and ACh3.0 fluorescence aligned to licks occurring between consummatory licking bouts (i.e., unrewarded licks). Gray: 95% confidence interval. **h-j**, Latency of first rewarded lick from solenoid valve opening (**h**; $P = 0.52$), fraction of rewards consumed within 1 s of valve opening (**i**; $P = 0.14$) and number of consummatory licks per reward delivery (**j**; $P = 0.59$) during the first (early) and last (late) quartiles of each imaging session in $n = 13$ mice suggest that the motivation

to consume rewards is stable. **k**, Mean reward-aligned DA and ACh responses imaged during the first (early; gray) and last (late; colored) quartiles of each imaging session are similar in amplitude and kinetics ($n = 13$ mice). **l**, Scatterplot of the mean amplitude of reward-evoked DA peaks (*left*; $P = 0.24$) and ACh troughs (*right*; $P = 0.74$) at the beginning (early) vs. end (late) of each imaging session ($n = 13$ mice). **m**, Scatterplot of the amplitude of individual DA peaks and concurrent ACh troughs imaged during reward (blue) and periods of immobility (orange) in one example recording session. Amplitude distribution for ACh (*top*) and DA (*right*) with overlap shown in gray. **n**, Mean distribution of DA peak (*left*) and ACh trough (*right*) amplitudes for all mice ($n = 13$) normalized to the mode of reward distributions showing considerable overlap between reward and immobility states. **o**, *Left*, power spectrum of DA signal recorded in the DLS during immobility in $n = 10$ female mice (black) and $n = 8$ male mice (magenta). *Right*, Area under the curve of DA power spectra in the 0.5–4 Hz frequency band ($P = 0.65$). **p**, Same as **o**, for ACh ($P = 0.84$). Group means (\pm s.e.m.) in **h-j**, **o** and **p** are shown in black. Shaded regions in **d-g**, **k**, **o** and **p** denote s.e.m. Statistical comparisons are Student's paired t -tests in **h-j** and **l**, and Student's two-sample t -tests in **o** and **p**.

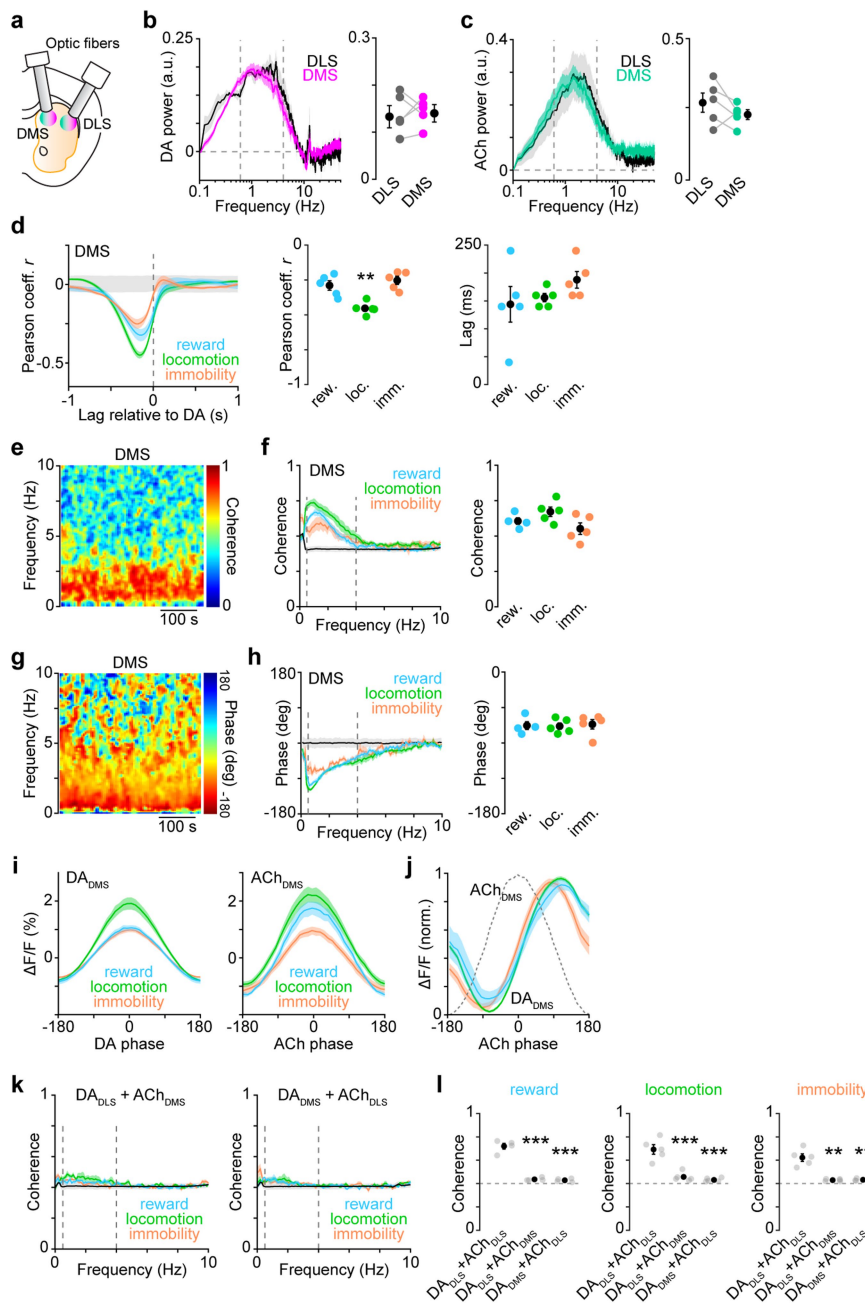


Extended Data Fig. 4 | Locomotion-evoked DA and ACh responses in the DLS. **a–b**, Experimental setup: virally-expressed rDA1m and ACh3.0 were imaged in the DLS (**a**) of mice head-fixed on a transparent cylindrical treadmill (**b**). **c**, Example rDA1m and ACh3.0 fluorescence from 2 separate mice during immobility (*left*) and spontaneous locomotion on the treadmill (*right*). **d**, Mean standard deviation of photometry signal during immobility and locomotion for ACh3.0 (*top*; $P = 6.5 \times 10^{-8}$, Student's paired *t*-test) and rDA1m (*bottom*; $P = 3.6 \times 10^{-4}$; Student's paired *t*-test). Group mean (\pm s.e.m.) shown in black ($n = 13$ mice). **e**, *Left*, mean ACh (*top*) and DA (*bottom*) power density spectrum during locomotion ($n = 13$ mice). *Right*, Area under the curve (AUC) in 0.5–4 Hz frequency band. Group mean (\pm s.e.m.) shown in black. **f**, Heatmap of mean ACh3.0 (*top*) and rDA1m (*bottom*) fluorescence aligned to momentary peaks in treadmill acceleration during locomotion across mice. **g**, Group-averaged ACh3.0 (*top*) and rDA1m (*bottom*) fluorescence aligned to acceleration peaks

stratified into tertiles according to acceleration magnitude. ACh and DA levels co-vary with acceleration magnitude. ACh levels peaking near acceleration maxima, whereas DA levels dip shortly before and crest shortly after acceleration maxima. **h**, Mean cross-correlation between treadmill acceleration and either ACh3.0 (teal) or rDA1m (magenta) fluorescence ($n = 13$ mice). **i**, Mean treadmill acceleration at different phases of periodic ACh fluctuations (dashed teal line) in $n = 13$ mice. During locomotion, periodic ACh fluctuations occur in phase with positive treadmill acceleration. Note that periodic ACh fluctuations during immobility are not associated with movements of the treadmill. **j**, Same as **i** for DA fluorescence. Note that DA fluctuations are phase-delayed relative to treadmill acceleration during locomotion, and not associated with micro-movements of the treadmill during immobility. Shaded regions in **e**, **g–j** denote s.e.m.



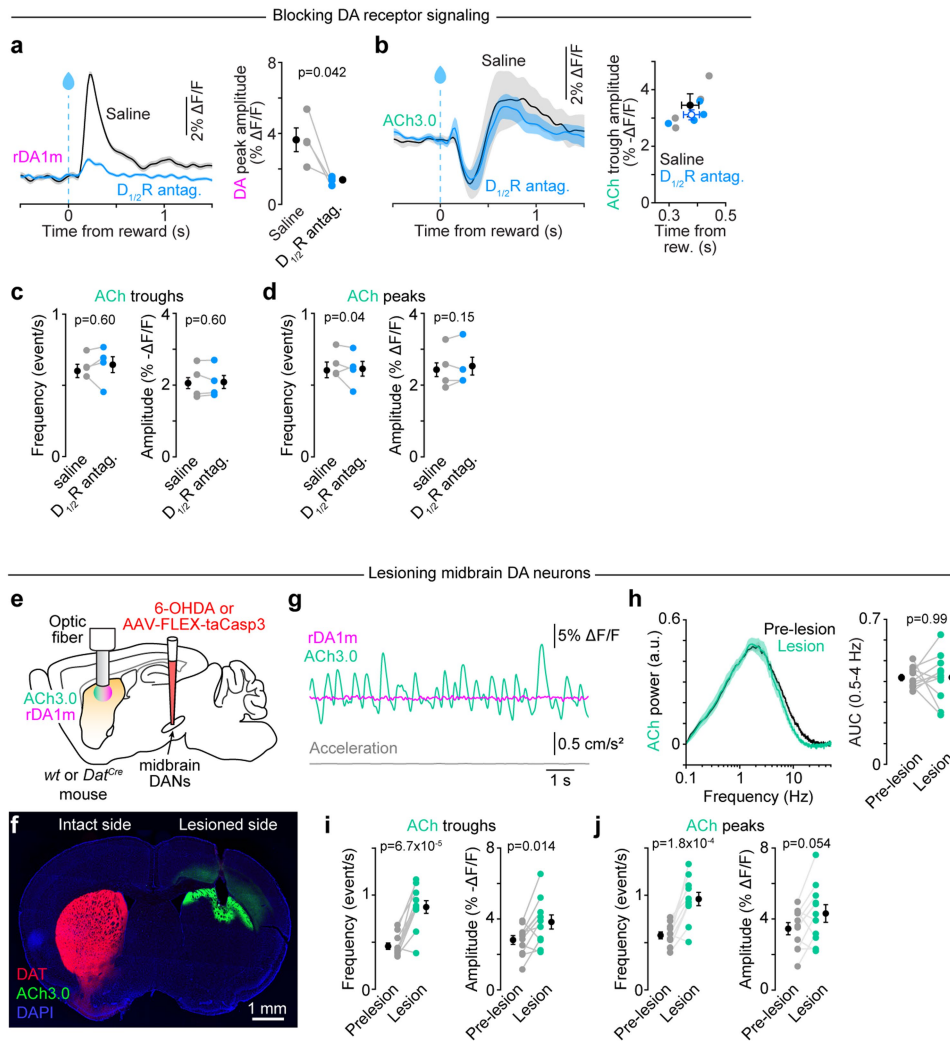
Extended Data Fig. 5 | Spontaneous fluctuations in striatal DA and ACh in unrestrained mice. **a**, Simultaneous photometry recording of rDA1m (magenta) and ACh3.0 (teal) fluorescence from a mouse in an open field arena. **b**, Mean cross-correlation between simultaneously recorded DA and ACh during locomotion (green) and immobility (orange) in $n = 4$ mice. **c**, Peak correlation coefficient between DA and ACh ($P = 0.93$) during immobility and locomotion ($n = 4$ mice). **d**, Same as **c** for time lag of negative cross-correlation peak ($p = 0.06$). **e**, Example coherence between DA and ACh signals across frequency and time domains during a recording in an open field arena. **f**, *Left*, mean coherence between DA and ACh at different frequencies ($n = 4$ mice). Vertical lines depict 0.5 and 4 Hz. *Right*, median coherence in 0.5–4 Hz frequency band in individual mice ($P = 0.25$). **g–h**, Same as **e–f** for phase offset between DA and ACh ($P = 0.93$). **i**, Mean DA fluorescence at different phases of periodic DA fluctuations in the 0.5–4 Hz frequency band ($n = 4$ mice). **j**, Same as **h** for ACh fluorescence. **k**, Peak-normalized DA fluorescence vs. phase of periodic ACh fluctuations (gray dotted line) in 0.5–4 Hz frequency band during locomotion (green) and immobility (orange). Group means (\pm s.e.m.) in **c**, **d**, **f** and **h** shown in black. Shaded areas in **b**, **f**, **h–k** reflect s.e.m. All statistical comparisons are Student's paired t -tests.



Extended Data Fig. 6 | DA and ACh levels also fluctuate periodically in DMS.

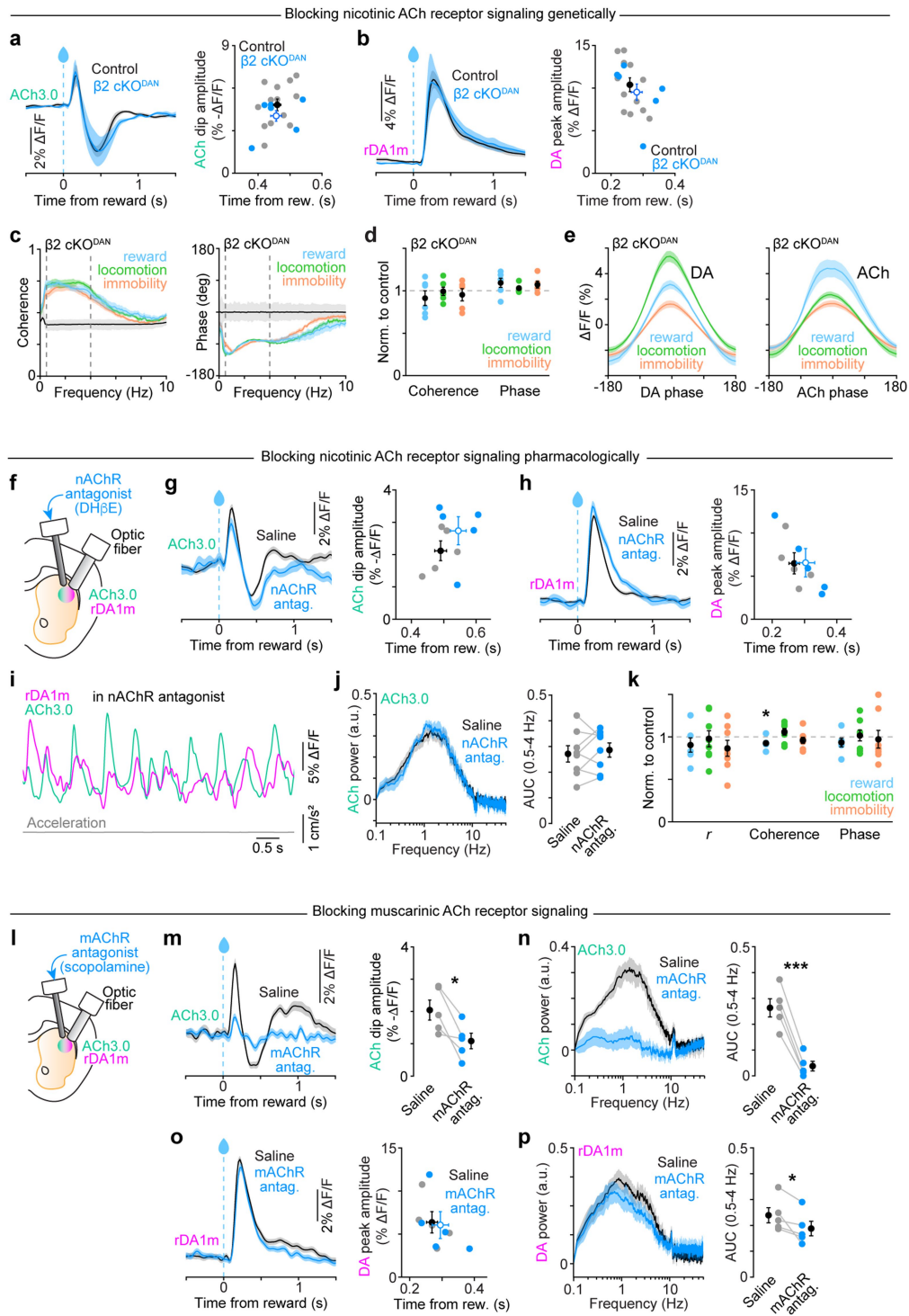
a, Experimental setup. **b**, *Left*, mean power spectrum of DA signal recorded simultaneously from DMS (magenta) and DLS (black) during immobility in $n = 5$ mice. *Right*, area under the DA power spectra in the 0.5–4 Hz frequency band in DMS and DLS. Group averages (\pm s.e.m.) shown in black ($p = 0.8$, Student's paired t -test). **c**, Same as **b** for ACh ($p = 0.3$). **d**, *Left*, mean cross-correlation between DA and ACh in DMS across different behavioral states. *Middle*, peak correlation coefficient (Pearson's r) in individual mice. Group averages (\pm s.e.m.) shown in black (** $p = 0.006$ vs. reward and immobility, one-way balanced ANOVA, Dunn's multiple comparisons; $n = 5$ mice). *Right*, time lag of negative cross-correlation peak ($p = 0.4$, one-way balanced ANOVA). **e**, Magnitude of coherence between DA and ACh in DMS across frequency and time domains for an example recording. **f**, *Left*, mean coherence at different frequencies across behavioral states ($n = 5$ mice). Vertical lines depict 0.5 and 4 Hz. *Right*, median coherence in 0.5–4 Hz frequency band in individual mice. Group averages

(\pm s.e.m.) shown in black ($p = 0.09$, one-way unbalanced ANOVA; $n = 5$ mice). **g**, Same as **e** for phase offset between DA and ACh in DMS. **h**, Same as **f** for phase offset between DA and ACh in DMS ($p = 0.2$, one-way unbalanced ANOVA). **i**, *Left*, mean DA fluorescence at different phase of DA fluctuations in the 0.5–4 Hz frequency band in DMS. *Right*, same for ACh fluorescence vs. phase of ACh fluctuations. **j**, Peak-normalized DA fluorescence vs. phase of ACh in DMS. **k**, *Left*, mean coherence between simultaneously recorded DA_{DLS} and ACh_{DMS} ($n = 5$ mice). *Right*, same for coherence between DA_{DMS} and ACh_{DLS}. **l**, Median coherence in 0.5–4 Hz band in individual mice. Group averages (\pm s.e.m.) shown in black (reward: DA_{DLS}+ACh_{DMS} $p = 8.14 \times 10^{-7}$; DA_{DMS}+ACh_{DLS} $p = 6.07 \times 10^{-7}$; locomotion: DA_{DLS}+ACh_{DMS} $p = 7.46 \times 10^{-5}$; DA_{DMS}+ACh_{DLS} $p = 6.07 \times 10^{-5}$; immobility: DA_{DLS}+ACh_{DMS} $p = 0.004$; DA_{DMS}+ACh_{DLS} $p = 0.005$; all vs. DA_{DLS}+ACh_{DLS}, one-way unbalanced ANOVA, Dunn's multiple comparisons; $n = 5$ mice). Shaded areas in **b–d**, **f**, **h–k** reflect s.e.m.



Extended Data Fig. 7 | DA does not drive spontaneous fluctuations in ACh. a, *Left*, example session-averaged DA fluorescence aligned to solenoid valve opening for all uncued water deliveries followed within 1 s by consummatory licking after intra-striatal infusion of saline (black) or a cocktail of D1 and D2 receptor antagonists (blue). *Right*, mean reward-evoked DA amplitude ($n = 4$ mice). **b,** *Left*, same as **a** for ACh. *Right*, scatter plot of mean reward-evoked ACh dip amplitude and timing in mice infused with saline or D1/2R antagonists (amplitude: $p = 0.2$; timing: $p = 0.9$, both vs. saline). **c,** Frequency (*left*) and amplitude (*right*) of spontaneous dips in ACh fluorescence during immobility ($n = 4$ mice). **d,** Same as **c** for peaks in ACh. **e,** Experimental preparation to lesion midbrain DA neurons (DANs) unilaterally while imaging DA and ACh in the DLS ipsilaterally. DANs were lesioned using either 6OHDA infusions in wild type mice ($n = 7$), or AAV-mediated expression of Cre-dependent caspase-3 (AAV-FLEX-

taCasp3) in the midbrain DANs of *Dat*^{Cre} mice ($n = 4$). **f,** Epifluorescence image of ACh3.0 (green) and DA transporter (DAT; red) immunofluorescence overlaid with DAPI nuclear stain (blue) in a coronal section from a *Dat*^{Cre} mouse injected with AAV-FLEX-taCasp3 into the right midbrain. Similar results were obtained in other 10 mice. **g,** Example DA (magenta) and ACh (teal) fluorescence following DAN lesion during immobility. **h,** *Left*, mean ACh power spectrum during immobility before (black) and after DAN lesion (teal; $n = 11$ mice). *Right*, ACh power area under the curve (AUC) in 0.5–4 Hz frequency band. **i,** Same as **c** before and after DAN lesion ($n = 11$ mice). Chronic DA depletion causes phasic dips in ACh to become larger and more frequent, hinting at a negative influence of DA on ACh release. **j,** Same as **d** before and after DAN lesion ($n = 11$ mice). Group means (\pm s.e.m.) in **a–d, h–j** are shown in black. Shaded areas in **a, b** and **h** reflect s.e.m. All statistical comparisons are Student's paired *t*-tests.

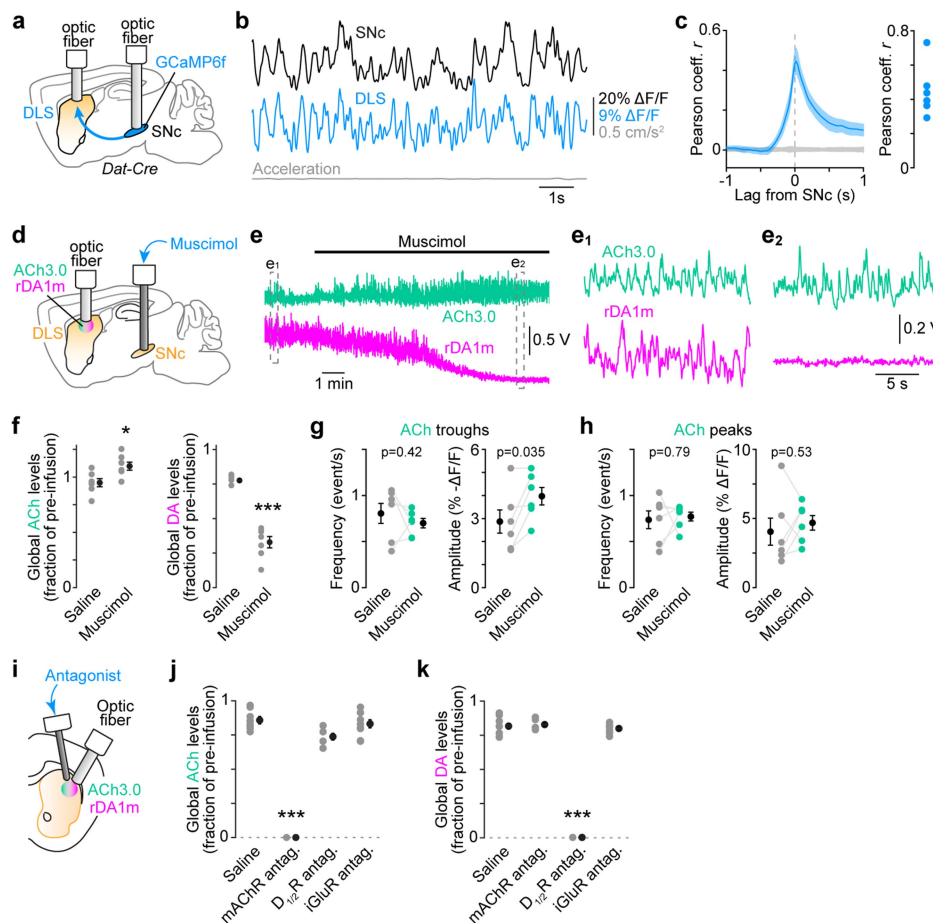


Extended Data Fig. 8 | See next page for caption.

Extended Data Fig. 8 | ACh signaling is not required for periodic DA

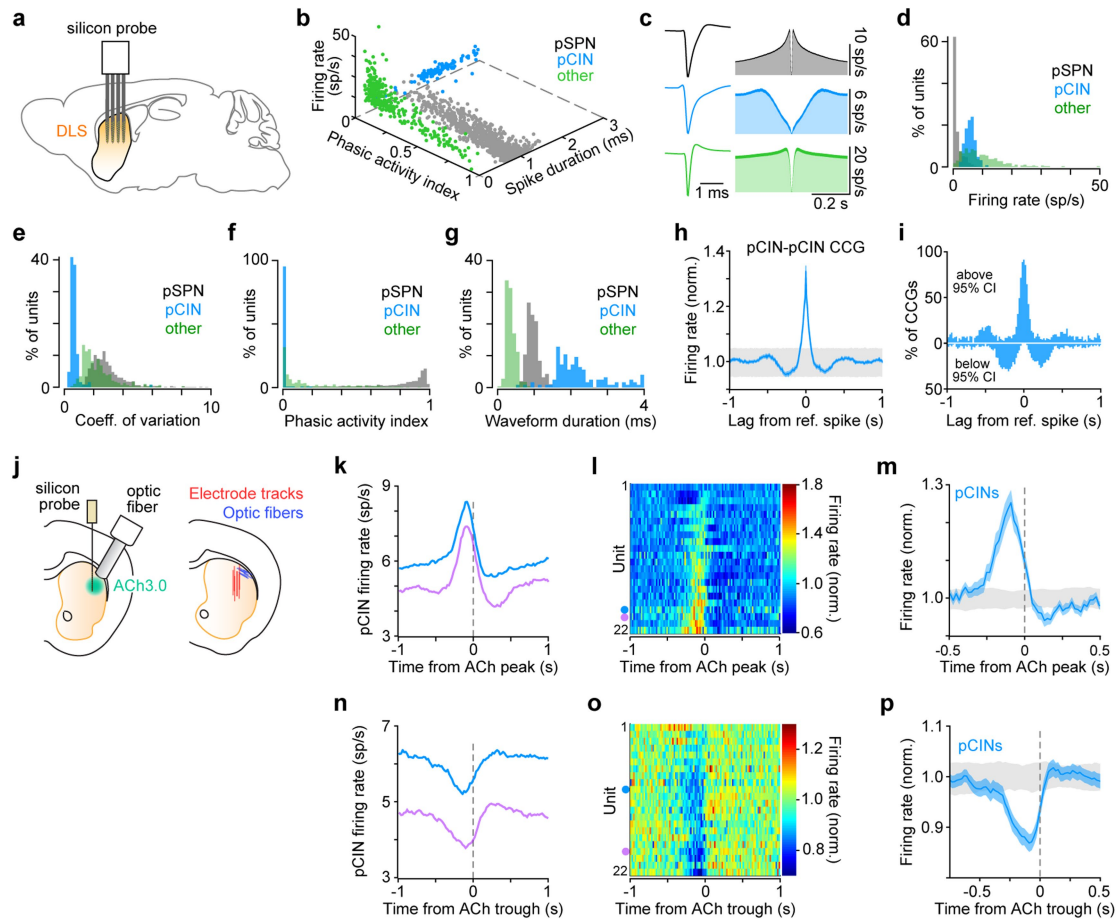
fluctuations. **a**, *Left*, example session-averaged ACh fluorescence aligned to solenoid opening for all uncued water deliveries followed within 1 s by consummatory licking in control (black) and $\beta 2$ cKO^{DAN} (blue) mice. *Right*, scatter plot of mean reward-evoked ACh dip amplitude and timing in control (gray; n = 13) and $\beta 2$ cKO^{DAN} (blue; n = 6) mice. Group means (\pm s.e.m.) overlaid (amplitude: p = 0.29; timing: p = 0.89, both vs. control, Student's two-sample *t*-test). **b**, *Left*, same as **a** for reward-evoked DA peak (amplitude: p = 0.58; timing, p = 0.33). **c**, *Left*, average coherence between DA and ACh signals in $\beta 2$ cKO^{DAN} mice (n = 6) at different frequencies during reward (blue), locomotion (green) and immobility (orange). Vertical lines depict 0.5 and 4 Hz. *Right*, same for phase offset. **d**, Median DA-ACh coherence and phase in 0.5–4 Hz band in $\beta 2$ cKO^{DAN} mice (n = 6) normalized to control mice across conditions (coherence: reward p = 0.9, locomotion p = 0.3, immobility p = 0.9; phase: reward p = 0.4, locomotion p = 0.6, immobility p = 0.2; all comparisons vs. control, Student's two-sample *t*-test). Group mean (\pm s.e.m.) shown in black. **e**, *Left*, average DA fluorescence at different phases of periodic DA fluctuations in the 0.5–4 Hz frequency band across behavioral states in $\beta 2$ cKO^{DAN} mice (n = 6 mice). *Right*, same for ACh fluorescence vs. phase of periodic ACh fluctuations. **f**, Experimental preparation for local pharmacological inhibition of nAChR signaling. **g**, Same as **a** after DLS infusion of saline (black) or the nAChR antagonist DH β E (blue;

amplitude: p = 0.4; timing: p = 0.13, both vs. saline, Student's paired *t*-test, n = 5 mice). **h**, Same as **g** for DA (amplitude: p = 0.9; timing: p = 0.15). **i**, Example DA (magenta) and ACh (teal) traces during infusion of DH β E. **j**, *Left*, mean ACh power spectrum during immobility following intra-striatal infusion of saline (black) or DH β E (blue; n = 8 mice). *Right*, ACh power area under the curve (AUC) in 0.5–4 Hz frequency band (p = 0.6, Student's paired *t*-test). **k**, Same as **d** for Pearson's correlation coefficient *r* (reward: p = 0.2, locomotion: p = 0.5, immobility: p = 0.06), coherence (reward: p = 0.04, locomotion: p = 0.6, immobility: p = 0.09) and phase (reward: p = 0.2, locomotion: p = 0.5, immobility: p = 0.6) in DH β E normalized to saline (all comparisons vs. saline, Student's paired *t*-test; n = 8 mice). **l**, Experimental preparation for local pharmacological inhibition of mAChR signaling in the DLS. **m**, *Left*, same as **g** following infusion of saline (black) or the mAChR antagonist scopolamine (blue). *Right*, amplitude of reward-evoked dip in ACh fluorescence (p = 0.02; n = 5 mice). **n**, same as **j** after infusion of saline or mAChR antagonist (p = 2.5×10^{-4} , Student's paired *t*-test; n = 5 mice). This effect confirms that scopolamine reaches the volume of tissue imaged by the fiber optic. **o**, Same as **m** for DA (amplitude: p = 0.6, timing: p = 0.09; n = 5 mice). **p**, Same as **n** for DA (p = 0.048). This effect is consistent with the role of facilitatory effects of presynaptic mAChRs on DAN axons (see ref. 31). Shaded areas in **a**, **b**, **c**, **e**, **g**, **h**, **j** and **m–p** reflect s.e.m.



Extended Data Fig. 9 | Midbrain DAN activity underlies periodic fluctuations in striatal DA. **a**, Experimental preparation for simultaneously imaging the activity of DANs in the SNc and their axons in the DLS. **b**, Example photometry recording of GCaMP6f in the SNc (black) and DLS (blue) during immobility. **c**, *Left*, average (\pm s.e.m. shown as shaded region) cross-correlation between SNc and DLS signals during immobility in $n = 6$ mice. 95% confidence interval shown in gray. *Right*, peak correlation coefficient between SNc and DLS signals. Group mean (\pm s.e.m.) in black. **d**, Experimental preparation for pharmacological silencing of SNc while imaging of rDA1m and ACh3.0 in the DLS. **e**, *Left*, Example continuous recording of ACh3.0 (teal) and rDA1m (magenta). Black line depicts muscimol infusion. *Right*, Detail of dashed boxes showing ACh and DA fluctuations during immobility before (**e**₁) and following (**e**₂) infusion of muscimol. Note that muscimol abolishes phasic DA transients as well as ‘global’ DA levels in the DLS, whereas ACh global levels and phasic transients persist. **f**, Average global ACh and DA fluorescence during immobility after infusion of saline and muscimol. Group mean (\pm s.e.m.) shown in black (ACh: $p = 0.021$; DA: $p = 0.0001$, Student’s paired t -test; $n = 6$ mice). **g**, Frequency (*left*) and amplitude (*right*) of spontaneous dips in ACh fluorescence recorded during immobility after infusion of saline (gray) or muscimol (teal). Group mean (\pm s.e.m.) shown in black ($n = 6$ mice). p -values (Student’s paired t -tests) indicated in figure.

h, Same as **g** for peaks in ACh fluorescence. Collectively, these data confirm that spontaneous DA fluctuations in the DLS are driven by the somatic activity of midbrain DANs, whereas spontaneous ACh transients do not require DAN activity. **i**, Experimental preparation for local pharmacological inhibition of neurotransmitter receptors in the DLS. **j**, Average global ACh fluorescence measured during immobility after intra-striatal infusion of saline, the mAChR antagonist scopolamine ($p = 6.9 \times 10^{-6}$; $n = 5$ mice), the D1/2R antagonists SCH23390 and sulpiride ($p = 0.24$; $n = 4$ mice) or the iGluR antagonists NBQX and APV ($p = 0.41$; $n = 8$ mice; all comparisons are Student’s paired t -test vs. saline control). Data are expressed as a fraction of global ACh fluorescence pre-infusion. Group means (\pm s.e.m.) are shown in black. Note that mAChR antagonist blocks ACh3.0 (and therefore serves a positive control for maximal possible change in ACh signal) and that blocking iGluRs in the DLS does not significantly alter overall ACh3.0 fluorescence compared to saline, suggesting that CINs continue to release ACh via spontaneous, cell-autonomous firing. **k**, Same as **j** for global DA fluorescence after infusion of saline, scopolamine ($p = 0.24$), D1/2R antagonists ($p = 1.1 \times 10^{-4}$) or iGluR antagonists ($p = 0.53$). Note that blocking iGluRs in the DLS does not alter overall rDA1m fluorescence either, suggesting that DA axons continue to release DA.



Extended Data Fig. 10 | Characterization of electrophysiological recordings in the DLS. **a**, Experimental preparation for acute *in vivo* extracellular recordings in the DLS. **b**, Scatter plot of spike properties used to distinguish units as putative SPNs (pSPNs; gray), putative CINs (pCINs; blue), or other putative interneurons (green). **c**, Average waveform (left) and auto-correlograms (right) for pSPNs (black), pCINs (blue), and other neurons (green). **d–g**, Distribution of firing rates (**d**), coefficient of variation of inter-spike intervals (**e**), phasic activity index (**f**), and waveform duration for pSPNs (black), pCINs (blue), and other neurons (green). **h**, Mean (\pm s.e.m.) pCIN-pCIN cross correlogram (CCG) computed from all units shown in Fig. 4c ($n = 157$ pairs). 95% confidence interval shown in gray. **i**, Proportion of CCGs from Fig. 4c with firing rates above or below the 95%

confidence interval (bin size: 20 ms). **j**, *Left*, experimental preparation for simultaneous ACh photometry and acute *in vivo* extracellular recordings from the DLS. *Right*, location of all recovered fiber optic implant tips (blue) and electrode tracks (red) in the DLS merged across anterior-posterior levels +0.5 to 0.75 mm relative to bregma. **k**, Mean firing rate of two simultaneously recorded pCIN units aligned to ACh fluorescence peaks during immobility. **l**, Instantaneous (mean normalized) firing rate of pCINs ($n = 22$) aligned to ACh fluorescence peaks during immobility. Dots indicate units shown in **k**. **m**, Average firing rate (normalized to mean; \pm s.e.m. shown in shaded region) of all pCINs shown in **l**. 95% confidence interval shown in gray. **n–p**, Same as **k–m** aligned to ACh fluorescence troughs.

Reporting Summary

Nature Portfolio wishes to improve the reproducibility of the work that we publish. This form provides structure for consistency and transparency in reporting. For further information on Nature Portfolio policies, see our [Editorial Policies](#) and the [Editorial Policy Checklist](#).

Statistics

For all statistical analyses, confirm that the following items are present in the figure legend, table legend, main text, or Methods section.

n/a Confirmed

- The exact sample size (n) for each experimental group/condition, given as a discrete number and unit of measurement
- A statement on whether measurements were taken from distinct samples or whether the same sample was measured repeatedly
- The statistical test(s) used AND whether they are one- or two-sided
Only common tests should be described solely by name; describe more complex techniques in the Methods section.
- A description of all covariates tested
- A description of any assumptions or corrections, such as tests of normality and adjustment for multiple comparisons
- A full description of the statistical parameters including central tendency (e.g. means) or other basic estimates (e.g. regression coefficient) AND variation (e.g. standard deviation) or associated estimates of uncertainty (e.g. confidence intervals)
- For null hypothesis testing, the test statistic (e.g. F , t , r) with confidence intervals, effect sizes, degrees of freedom and P value noted
Give P values as exact values whenever suitable.
- For Bayesian analysis, information on the choice of priors and Markov chain Monte Carlo settings
- For hierarchical and complex designs, identification of the appropriate level for tests and full reporting of outcomes
- Estimates of effect sizes (e.g. Cohen's d , Pearson's r), indicating how they were calculated

Our web collection on [statistics for biologists](#) contains articles on many of the points above.

Software and code

Policy information about [availability of computer code](#)

Data collection

Photometry recordings were performed using Wavesurfer 0.981 software (Janelia) using MATLAB 2018a (MathWorks). Signals were acquired as analog inputs to a National Instruments data acquisition board (PCIe-6353) and breakout terminal block (BNC-2090). Electrophysiology recordings were performed using OpenEphys software. Behavioral data were acquired using custom code in MATLAB 2018a. Details on data collection for each experiment are provided in the Methods.

Data analysis

Photometry data processing was performed using a custom MATLAB (MathWorks) pipeline. Electrophysiology data was processed using Kilosort2 ([www.github.com/MouseLand/Kilosort2](https://github.com/MouseLand/Kilosort2)) and Phy (<https://phy.readthedocs.io/en/latest>). Open field data was processed using EthoVision XT 11.5 software. Quantification of photometry, electrophysiology, and behavioral data was carried out in MATLAB 2018a using custom-code as well as Buzcode MATLAB analysis tools (<https://github.com/buzsakilab/buzcode>) and Chronux toolbox (<http://chronux.org>). Graphing and statistical analysis was done in MATLAB 2018a. Details on quantification and data analysis for each experiment are provided in the Methods. All custom analysis code is available on GitHub (<https://github.com/ackrok>).

For manuscripts utilizing custom algorithms or software that are central to the research but not yet described in published literature, software must be made available to editors and reviewers. We strongly encourage code deposition in a community repository (e.g. GitHub). See the Nature Portfolio [guidelines for submitting code & software](#) for further information.

Data

Policy information about [availability of data](#)

All manuscripts must include a [data availability statement](#). This statement should provide the following information, where applicable:

- Accession codes, unique identifiers, or web links for publicly available datasets
- A description of any restrictions on data availability
- For clinical datasets or third party data, please ensure that the statement adheres to our [policy](#)

The data that support the findings of this study are available from the corresponding author upon request.

Human research participants

Policy information about [studies involving human research participants and Sex and Gender in Research](#).

Reporting on sex and gender	N/A
Population characteristics	N/A
Recruitment	N/A
Ethics oversight	N/A

Note that full information on the approval of the study protocol must also be provided in the manuscript.

Field-specific reporting

Please select the one below that is the best fit for your research. If you are not sure, read the appropriate sections before making your selection.

- Life sciences Behavioural & social sciences Ecological, evolutionary & environmental sciences

For a reference copy of the document with all sections, see [nature.com/documents/nr-reporting-summary-flat.pdf](https://www.nature.com/documents/nr-reporting-summary-flat.pdf)

Life sciences study design

All studies must disclose on these points even when the disclosure is negative.

Sample size	We did not make a priori calculations of sample size. Our sample sizes are consistent with or larger than similar publications using comparable methods (see refs. 4,14,16,18,19,23).
Data exclusions	3 out of 16 dual DA-ACh photometry recordings were excluded from analyses as they did not display significant fluorescent fluctuations in either DA and/or ACh during periods of immobility, movement or in response to uncued rewards; post-hoc immunohistochemical analyses confirmed poor viral expression of fluorescent sensor(s) under the fiber optic. Neuronal spiking data were only considered if they met criteria for high-quality single units prior to analysis, as detailed in Methods.
Replication	Results were consistently observed in multiple experimental subjects in separate experimental cohorts.
Randomization	Animals were not randomly assigned to experimental groups as comparisons were either made within subjects (paired comparisons; e.g., saline vs. D1R/D2R antagonist infusions in the same animal, or before and after DA neuron lesions in the same animal), or between mice of different genotypes (e.g., control vs. cKO mice).
Blinding	Blinding to experimental condition is not relevant in this study, as the outcome of photometry and electrophysiology experiments can only be determined after the conclusion of recording sessions during post-hoc analyses, which are applied identically to all experimental groups using automated methods.

Reporting for specific materials, systems and methods

We require information from authors about some types of materials, experimental systems and methods used in many studies. Here, indicate whether each material, system or method listed is relevant to your study. If you are not sure if a list item applies to your research, read the appropriate section before selecting a response.

Materials & experimental systems

Methods

n/a	Involvement
<input type="checkbox"/>	<input checked="" type="checkbox"/> Antibodies
<input checked="" type="checkbox"/>	<input type="checkbox"/> Eukaryotic cell lines
<input checked="" type="checkbox"/>	<input type="checkbox"/> Palaeontology and archaeology
<input type="checkbox"/>	<input checked="" type="checkbox"/> Animals and other organisms
<input checked="" type="checkbox"/>	<input type="checkbox"/> Clinical data
<input checked="" type="checkbox"/>	<input type="checkbox"/> Dual use research of concern

n/a	Involvement
<input checked="" type="checkbox"/>	<input type="checkbox"/> ChIP-seq
<input checked="" type="checkbox"/>	<input type="checkbox"/> Flow cytometry
<input checked="" type="checkbox"/>	<input type="checkbox"/> MRI-based neuroimaging

Antibodies

Antibodies used

Chicken anti-GFP (polyclonal), Abcam, AB13970 (for IHC)
 Rabbit anti-DsRed (polyclonal), Takara, 632496 (for IHC)
 Rat anti-DAT (monoclonal), Millipore, MAB369 (for IHC)
 Goat anti-chicken Alexa Fluor 488, ThermoFisher, #A11039
 Goat anti-rabbit Alexa Fluor 568, ThermoFisher, #A11036
 Goat anti-rat Alexa Fluor 647, ThermoFisher, #A21247

Validation

Commercial antibodies were validated by the manufacturer, prior research studies, and expression patterns consistent with known anatomical distribution. For example, the anti-DAT antibody strongly labels axons throughout the striatum, but not in brain areas known to not be innervated by DA neurons. Similarly, the anti-GFP and anti-DsRed antibodies show no labeling in brain regions that do not express either transgene, and show subcellular staining patterns consistent with the known distribution of the neurotransmitter sensors they target.

Animals and other research organisms

Policy information about [studies involving animals](#); [ARRIVE guidelines](#) recommended for reporting animal research, and [Sex and Gender in Research](#)

Laboratory animals

The following mouse strains were used: C57BL/6J wild type mice (Jackson Laboratory strain #000664), Nkx2.1-Cre; ChAT flox (C57BL/6J background; donated by Dr. Rob Machold, NYULH; but each line is individually available from Jackson Laboratory strains #016920 and #008661), DAT-ires-Cre knockin mice (C57BL/6J background; Jackson Laboratory strain #006660) and beta2 flox mice (C57BL/6J background; donated by Dr. Michale Crair, Yale). Experiments were carried out using mice heterozygous for Cre transgenes and, when applicable, homozygous for flox transgenes, between 8–24 weeks of age. Mice were housed (ambient temperature: 70 ± 2°C, humidity: 50 ± 10%) in groups under a reverse 12 h light-dark cycle (dark from 10 a.m. to 10 p.m.) with ad libitum access to food and water.

Wild animals

The study did not involve wild animals.

Reporting on sex

Experiments were carried out using both male and female mice. 54% of animals used for fiber photometry experiments were female. 50% of animals used for electrophysiological experiments were female.

Field-collected samples

The study did not involve samples collected from the field.

Ethics oversight

All animal procedures were carried out in accordance with protocols approved by the NYU Langone Health Institutional Animal Care and Use Committee.

Note that full information on the approval of the study protocol must also be provided in the manuscript.